Potential heat production from the Seagull and Teslin plutonic suites, southern Yukon: Geochemistry, geochronology, rock physical properties, and 3D geophysical inversion of Bouguer gravity data

Maurice Colpron*
Yukon Geological Survey

Nathan Hayward
Geological Survey of Canada

James L. Crowley
Boise State University

Colpron, M., Hayward, N. and Crowley, J.L., 2021. Potential heat production from the Seagull and Teslin plutonic suites, southern Yukon: Geochemistry, geochronology, rock physical properties, and 3D geophysical inversion of Bouguer gravity data. *In:* Yukon Exploration and Geology 2020, K.E. MacFarlane (ed.), Yukon Geological Survey, p.47–72.

Abstract

Cretaceous granitoid plutons of the Seagull and Teslin plutonic suites, east of Teslin, are evaluated for their potential radiogenic heat production. The Seagull suite comprises ultra-fractionated, A-type granites dated at *ca.* 103–101 Ma that have anomalous average heat production values (*A*) of 7.9 to 9.9 μW/m^3. The Teslin suite is older (*ca.* 121–109 Ma) and characterized by more intermediate granodiorite compositions that mostly have average *A* values of 2.0 μW/m^3, closer to global averages. Locally, anomalous *A* values of 4.5 to 11.4 μW/m^3 are associated with younger (*ca.* 110–108 Ma), more evolved granitic phases of the Teslin suite. The 3D inversion of Bouguer gravity data provides models that constrain the subsurface density character and extents of the Hake and Seagull batholiths, and estimated volumes of ~4624 and 2744 km^3, respectively. The combination of these results suggests that potential heat energy of ~36.5 MWt may be contained in the Hake batholith, and as much as 27.2 MWt in the Seagull batholith.

* *maurice.colpron@yukon.ca*

Introduction

As part of the Yukon Geological Survey's geothermal research program, a regional assessment of the potential radiogenic heat production from granitoid plutons was done using a compilation of published and archival lithogeochemical data for southern Yukon (Friend and Colpron, 2017; Yukon Geological Survey, 2020a). This analysis showed that Cretaceous plutons of the Seagull suite (103–96 Ma), which intrude the Yukon-Tanana terrane east of Teslin (Fig. 1), are some of the most radiogenic plutons in Yukon, with potential heat production values locally exceeding 10 $\mu W/m^3$ (Friend and Colpron, 2017). This region coincides with some of the shallowest Curie point depths mapped in Yukon, also suggesting potentially higher crustal heat flow (Witter and Miller, 2017; Witter *et al.*, 2018). To further investigate the geothermal potential of the region, we visited plutons of the Seagull plutonic suite during the summer of 2019 and collected additional samples for lithogeochemical analysis and rock physical property measurements. Samples from the older Teslin plutonic suite (123–108 Ma), which intrudes the western Yukon-Tanana terrane near Teslin, were also collected to fill a gap in the lithogeochemical data compilation.

In this paper, we summarize the geological and geochemical characteristics of plutons of the Seagull and Teslin plutonic suites, evaluate their potential radiogenic heat production, and present new chemical abrasion–thermal ionization mass spectrometry (CA-TIMS) U-Pb zircon dates for 4 of these plutons. The subsurface density character and extent of the Hake and Seagull batholiths—the most radiogenic plutons in the region—are modeled using 3D geophysical inversion of Bouguer gravity data building on the strategy of Hayward (2019). The 3D geometries and volume estimates derived from the gravity inversion are combined with radiogenic heat values to estimate the potential heat energy contained in these granitic bodies.

Geological Setting

The Seagull plutonic suite (103–96 Ma) comprises a series of highly fractionated A-type granites associated with tin (Sn), tungsten (W), tantalum (Ta) and niobium (Nb) mineralization in southern Yukon (Abbott, 1981; Liverton and Alderton, 1994; Liverton *et al.*, 2005; Liverton, 2016). East of Teslin, the Seagull, Hake and Thirtymile Range plutons define a northwest-trending belt of intrusions along the eastern edge of the Yukon-Tanana terrane, near its boundary with the Cassiar terrane (Fig. 1; Rasmussen, 2013; Colpron *et al.*, 2016). This younger, mid-Cretaceous suite of highly fractionated granites is flanked on both sides by older, Early Cretaceous calc-alkaline diorite and granodiorite plutons of the Teslin suite (123–115 Ma) to the west and the Cassiar suite (115–104 Ma) to the east (intruded into Cassiar terrane; Fig. 1). These three distinct Cretaceous plutonic suites apparently occur within distinct fault panels, although the Nisutlin River and Hidden Lake faults are both plugged by Early Jurassic plutons of the Lokken suite (195–184 Ma; Fig. 1; Roots *et al.*, 2004; Sack *et al.*, 2020), and the Ram Creek fault is truncated to the south by the Cassiar fault, which is inferred to have developed during or shortly after emplacement of the Cassiar batholith at *ca.* 110–95 Ma (Gabrielse *et al.*, 2006). Thus, intrusion of the Seagull and Teslin suites occurred after development of the regional structures affecting the Yukon-Tanana terrane in this area. Older phases of the Teslin suite are locally deformed in the Deadman Creek batholith (Gordey *et al.*, 1998; this study), and development of the structural fabric is possibly related with displacement along the nearby Teslin fault (Fig. 1).

The Seagull plutonic suite is primarily composed of reduced, ilmenite-bearing, biotite leucogranite to monzogranite, but also includes local lepidolite–(zinnwaldite)–albite–fluorite–topaz leucogranite and rare hornblende lamprophyre (Liverton and Alderton, 1994; Rasmussen, 2013). The main exposures of the Seagull suite in southern Yukon occur in the Seagull and Hake batholiths, and the Thirtymile Range pluton, and satellite stocks and dikes (Fig. 1). The granite is texturally variable, ranging from fine to coarse grained, from equigranular to K-feldspar porphyritic,

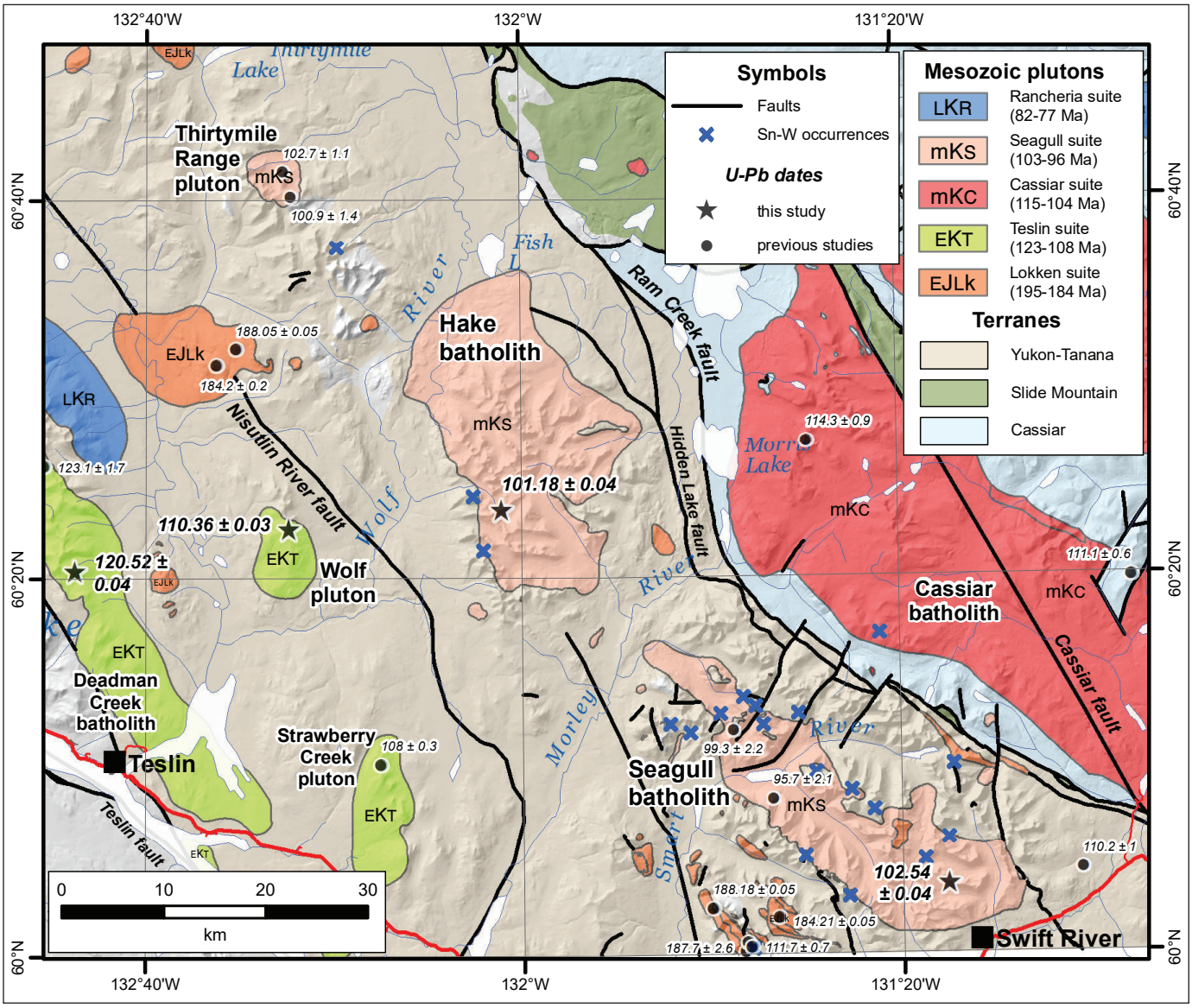

Figure 1. *Simplified geological map of the Teslin–Wolf Lake area, southern Yukon, showing the distribution of Mesozoic plutons and associated Sn-W occurrences (geology after Yukon Geological Survey, 2020b; mineral occurrences from Yukon Geological Survey, 2020c). Previous U-Pb dates for Jurassic and Cretaceous plutons are from the Yukon Geological Survey (2020d) compilation. New U-Pb dates presented here are shown by stars.*

and locally megacrystic (Fig. 2a–c). The K-feldspar (microcline) is commonly perthitic, and rapakivi texture is partially developed in parts of the Hake batholith (Fig. 2d). Smoky quartz is common in coarser grained phases (Fig. 2a). Miarolitic cavities with tourmaline–fluorite ± beryl ± topaz fills, pegmatite pods and quartz–tourmaline orbicules with aplitic margins indicate a shallow emplacement depth for plutons of the Seagull suite (Liverton and Alderton, 1994; Rasmussen, 2013; Liverton, 2016). The plutons are inferred to be connected at depth and represent the apex of a large, regional batholith approximately 100 km long by 20 km wide (Liverton *et al.*, 2005).

The Teslin suite, near the town of Teslin, was also investigated for its potential heat generation. In our study area, the Teslin suite comprises the Deadman Creek batholith and the Wolf and Strawberry Creek plutons (Fig. 1). The Teslin suite is composed mainly

of biotite ± hornblende diorite and granodiorite. The rocks are fine to coarse grained, and locally very coarse grained, and vary from equigranular to K-feldspar porphyritic to locally pegmatitic. Medium to coarse-grained, equigranular, biotite granite and leucogranite are common in the Strawberry Creek and Wolf plutons (Fig. 2e). Fine-grained hornblende diorite occurs locally along the eastern margin of the Deadman Creek batholith. Older diorite and granodiorite phases in the Deadman Creek batholith are locally foliated (Fig. 2f), but in general granodiorite and granite phases are undeformed.

Geochronology

Previous U-Pb zircon dates of the Teslin suite are presented in Gordey *et al.* (1998). These results were obtained using multi-grain zircon fractions that were air-abraded and analyzed by ID-TIMS at the Geological Survey of Canada. For most samples, zircon fractions are discordant and generally yielded imprecise dates. An older, lineated granodiorite phase in the Deadman Creek batholith is dated at 123.1 ± 1.7 Ma, whereas Bt granite from the northern margin of the pluton is 109 ± 2 Ma (Gordey *et al.*, 1998). A sample of coarse-grained biotite granite from the Strawberry Creek pluton is 108.0 ± 0.3 Ma (Fig. 1).

Zircons from the Seagull suite were previously analyzed by LA-ICPMS at the University of British Columbia. Two samples of granite from the northern part of the Seagull batholith yielded $^{206}Pb/^{238}U$ weighted mean dates of 95.7 ± 2.1 and 99.3 ± 2.2 Ma (Fig. 1; Mortensen *et al.*, 2006). In the Thirtymile Range pluton, a K-feldspar porphyritic granite yielded a $^{206}Pb/^{238}U$ weighted mean date of 102.7 ± 1.1 Ma, whereas an equigranular biotite granite phase is 100.9 ± 1.4 Ma (Fig. 1; Mortensen *et al.*, 2007).

We selected four samples of Cretaceous granitoid rocks for more precise analyses of single zircon crystals using the CA-TIMS method at Boise State University (Table 1; Appendix 1). Two samples of granite were collected from the Seagull and Hake batholiths (Seagull suite); for the Teslin suite, we collected a foliated granodiorite in the Deadman Creek batholith and a leucogranite in the Wolf pluton (Fig. 1). For each sample, zircon grains were first imaged by cathodoluminescence (CL) and selected spots were analyzed by laser ablation–inductively coupled mass spectrometry (LA-ICPMS; see Appendix 1 for methods; CL images are presented in Appendix 2 and LA-ICPMS data in Appendix 3). These results were then used to select zircon crystals for CA-TIMS. Weighted mean $^{206}Pb/^{238}U$ dates were calculated from equivalent dates (probability of fit [pof] >0.05) using Isoplot 3.0 (Ludwig, 2003). Errors on the weighted mean dates are given as ± *x* / *y* / *z*, where: *x* is the internal error based on analytical uncertainties only, including counting statistics, subtraction of tracer solution, and blank and initial common Pb subtraction; *y* includes the tracer calibration uncertainty propagated in quadrature; and *z* includes the ^{238}U decay constant uncertainty propagated in quadrature. Internal errors should be considered when comparing our dates with $^{206}Pb/^{238}U$ dates from other laboratories that used the same tracer solution or a tracer solution that was cross-calibrated using EARTHTIME gravimetric standards (Condon *et al.*, 2015). Errors including the uncertainty in the tracer calibration should be considered when comparing our dates with those derived from other geochronological methods using the U-Pb decay scheme (e.g., LA-ICPMS). Errors including uncertainties in the tracer calibration and ^{238}U decay constant should be considered when comparing our dates with those derived from other decay schemes (e.g., $^{40}Ar/^{39}Ar$, ^{187}Re-^{187}Os). Errors are given at 2σ.

Thirty-one zircon grains from 19MC-040, foliated granodiorite from the Deadman Creek batholith, yield LA-ICPMS dates between 132 ± 7 and 110 ± 5 Ma. Twenty-two dates yield a weighted mean of 120 ± 2 Ma (Mean Squared Weighted Deviation [MSWD] = 1.3, pof = 0.19). Six grains were analyzed by CA-TIMS. Four dates yield a weighted mean of 120.52 ± 0.04 / 0.07 / 0.15 Ma (MSWD = 0.8, pof = 0.48; Fig. 3a). This is the interpreted igneous crystallization age. One grain with a date of 120.70 ± 0.09 Ma is interpreted as containing an inherited component. One grain with a date of 119.82 ± 0.09 Ma is interpreted as having domains that suffered Pb loss despite chemical abrasion.

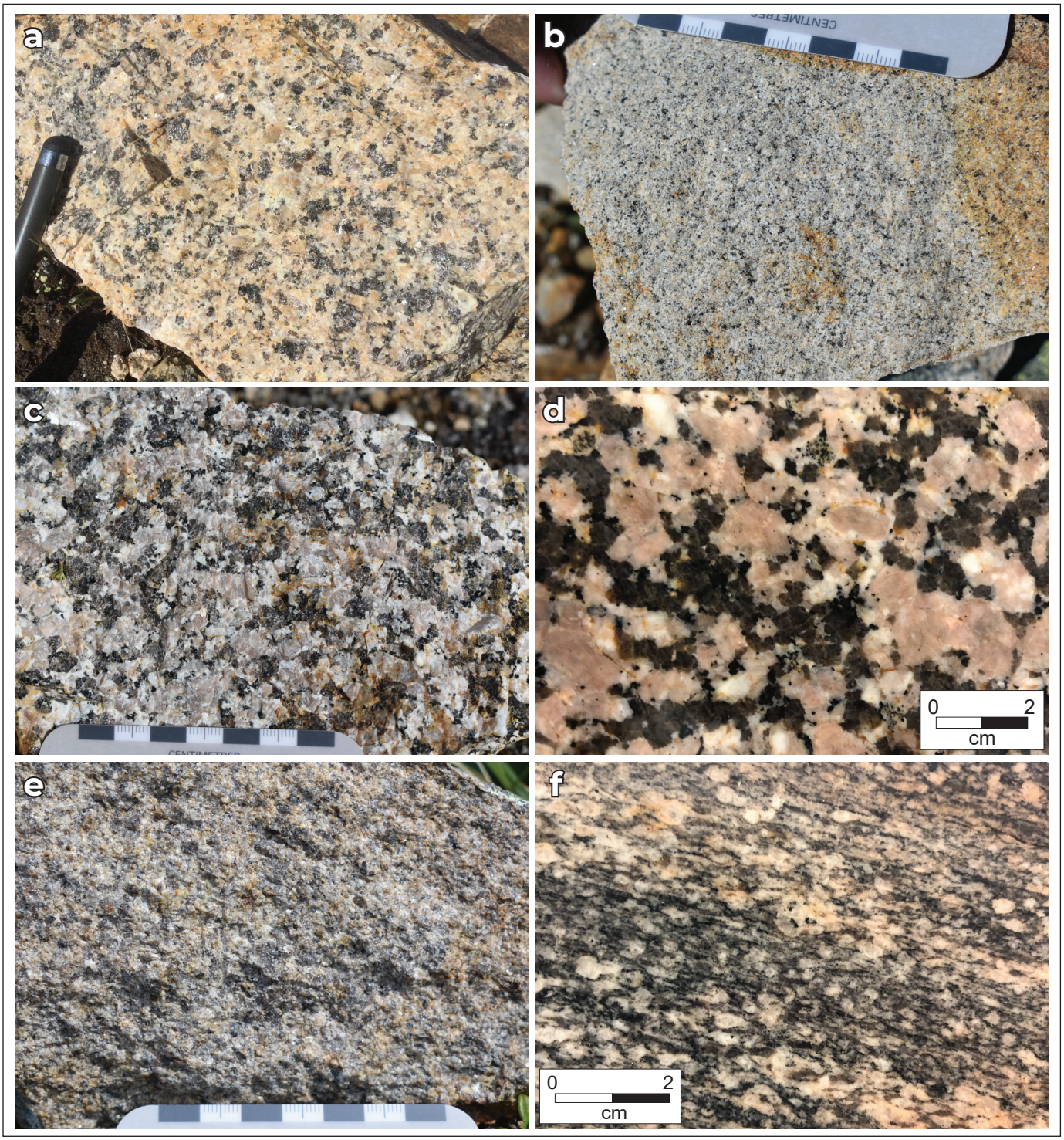

Figure 2. *Representative lithology of the Seagull, Hake and Wolf plutons.* **(a)** *coarse-grained, equigranular leucogranite from the southern part of the Seagull batholith. Note the coarse smoky quartz.* **(b)** *fine-grained biotite granite, central Seagull batholith.* **(c)** *coarse-grained, K-feldspar porphyritic, biotite granite from the Hake batholith. Note the smoky quartz.* **(d)** *partial development of rapakivi texture in the Hake batholith.* **(e)** *medium-grained, equigranular, biotite granite from the Wolf pluton.* **(f)** *foliation in granodiorite of the Deadman Creek batholith.*

Table 1. *CA-TIMS zircon U-Pb isotopic data.*

									Radiogenic Isotope Ratios					
	Th	^{206}Pb*	mol %	Pb*	Pb$_c$	^{206}Pb	^{208}Pb	^{207}Pb		^{207}Pb		^{206}Pb		corr.
Sample	U	x10^{-13} mol	^{206}Pb*	Pb$_c$	(pg)	^{204}Pb	^{206}Pb	^{206}Pb	% err	^{235}U	% err	^{238}U	% err	coef.
(a)	(b)	(c)	(c)	(c)	(c)	(d)	(e)	(e)	(f)	(e)	(f)	(e)	(f)	
19MC-040														
z1	0.550	1.0595	99.46%	56	0.48	3339	0.176	0.048532	0.150	0.126420	0.201	0.018901	0.073	0.788
z3	0.623	1.0438	99.60%	77	0.35	4509	0.199	0.048629	0.132	0.126524	0.185	0.018878	0.075	0.816
z2	0.636	0.6421	99.53%	66	0.25	3831	0.203	0.048692	0.148	0.126646	0.200	0.018872	0.072	0.809
z4	0.586	0.5822	99.34%	47	0.32	2754	0.187	0.048638	0.196	0.126495	0.245	0.018871	0.073	0.746
z5	0.445	0.9920	99.64%	81	0.30	4948	0.142	0.048516	0.119	0.126127	0.173	0.018863	0.071	0.849
z6	0.573	1.3062	99.72%	110	0.30	6483	0.183	0.048509	0.110	0.125427	0.165	0.018761	0.072	0.860
19MC-048														
z7	0.410	0.4584	99.39%	48	0.23	2973	0.131	0.048071	0.218	0.106500	0.260	0.016075	0.077	0.652
z2	0.567	2.0922	98.77%	25	2.14	1510	0.181	0.048034	0.143	0.106385	0.197	0.016070	0.074	0.824
z6	0.449	1.4114	99.59%	72	0.48	4429	0.144	0.048107	0.099	0.106437	0.157	0.016054	0.071	0.900
z3b	0.428	1.0407	99.87%	221	0.12	13565	0.137	0.048098	0.096	0.106298	0.153	0.016036	0.071	0.889
z3a	0.401	1.9700	99.92%	369	0.13	22790	0.128	0.048135	0.078	0.106378	0.138	0.016036	0.072	0.921
z5	0.294	2.3519	99.90%	290	0.19	18434	0.094	0.048150	0.071	0.106410	0.137	0.016036	0.075	0.944
z4	0.122	3.8832	99.96%	641	0.14	42877	0.039	0.048240	0.064	0.106558	0.130	0.016028	0.072	0.960
19MC-052														
z2	0.305	4.3695	99.94%	443	0.23	28093	0.098	0.048131	0.069	0.105205	0.132	0.015860	0.071	0.948
z4	0.414	1.3024	99.62%	76	0.42	4688	0.132	0.048124	0.118	0.105168	0.172	0.015857	0.071	0.846
z5	0.272	3.7587	99.93%	431	0.20	27577	0.087	0.048172	0.067	0.105190	0.132	0.015845	0.073	0.955
z1a	0.283	3.0042	99.91%	325	0.22	20744	0.091	0.048105	0.070	0.105013	0.134	0.015840	0.071	0.948
z1b	0.258	2.1049	99.91%	315	0.16	20253	0.082	0.048118	0.070	0.104929	0.133	0.015823	0.070	0.958
z6	0.296	2.0043	99.82%	158	0.30	10090	0.095	0.048100	0.085	0.104865	0.145	0.015819	0.071	0.914
z3	0.629	2.7527	99.91%	351	0.20	20420	0.201	0.048083	0.070	0.104802	0.133	0.015815	0.070	0.955
19MC054														
z6	0.811	1.0293	99.82%	183	0.15	10172	0.259	0.048328	0.098	0.115102	0.156	0.017282	0.071	0.895
z4	0.329	2.1726	99.92%	359	0.14	22587	0.105	0.048331	0.088	0.115024	0.144	0.017269	0.071	0.883
z5	0.532	0.9539	99.71%	105	0.23	6265	0.170	0.048344	0.115	0.115035	0.170	0.017265	0.071	0.859
z3	0.618	0.4530	99.51%	63	0.19	3669	0.198	0.048229	0.190	0.114750	0.239	0.017264	0.075	0.752
z2	0.578	0.9000	99.74%	118	0.19	6959	0.185	0.048294	0.106	0.114905	0.163	0.017264	0.071	0.891
z1	0.525	2.6265	99.93%	455	0.14	27189	0.168	0.048309	0.076	0.114925	0.137	0.017262	0.071	0.929

(a) z1, z2, etc. are labels for analyses composed of single zircon grains that were annealed and chemically abraded (Mattinson, 2005). Letters a and b denote fragments from the same grain.

(b) Model Th/U ratio calculated from radiogenic ^{208}Pb/^{206}Pb ratio and ^{207}Pb/^{235}U date.

(c) Pb* and Pbc are radiogenic and common Pb, respectively. mol % ^{206}Pb* is with respect to radiogenic and blank Pb.

d) Measured ratio corrected for spike and fractionation only. Fractionation correction for analyses done with tracer solution BSU1B is 0.18 ± 0.03 (1 sigma) %/amu (atomic mass unit) for single-collector Daly analyses, based on analysis of EARTHTIME ^{202}Pb-^{205}Pb ET2535 tracer solution. Fractionation correction for analyses done with tracer solution ET2535 is based on measurement of ^{202}Pb/^{205}Pb in the tracer solution.

(e) Corrected for fractionation and spike. Common Pb in zircon analyses is assigned to procedural blank with composition of ^{206}Pb/^{204}Pb = 18.04 ± 0.61%; ^{207}Pb/^{204}Pb = 15.54 ± 0.52%; ^{208}Pb/^{204}Pb = 37.69 ± 0.63% (1 sigma). ^{206}Pb/^{238}U and ^{207}Pb/^{206}Pb ratios corrected for initial disequilibrium in ^{230}Th/^{238}U using a D(Th/U) of 0.20 ± 0.05 (1 sigma).

(f) Errors are 2 sigma, propagated using algorithms of Schmitz and Schoene (2007) and Crowley *et al.* (2007).

(g) Calculations based on the decay constants of Jaffey *et al.* (1971). ^{206}Pb/^{238}U and ^{207}Pb/^{206}Pb dates corrected for initial disequilibrium in ^{230}Th/^{238}U using a D(Th/U) of 0.20 ± 0.05 (1 sigma).

Table 1 *continued. CA-TIMS zircon U-Pb isotopic data.*

	Isotopic Dates							
Sample	$^{207}Pb/^{206}Pb$	±	$^{207}Pb/^{235}U$	±	$^{206}Pb/^{238}U$	±	included in weighted mean?	
(a)	(g)	(f)	(g)	(f)	(g)	(f)		***Weighted Mean Calculations***
19MC-040								
z1	124.22	3.54	120.88	0.23	120.71	0.09		$^{206}Pb/^{238}U$ ± random (+tracer) [+decay constant]
z3	128.95	3.10	120.97	0.21	120.56	0.09	x	**120.52** **± 0.04** (0.07) [0.15]
z2	131.98	3.47	121.08	0.23	120.53	0.09	x	
z4	129.34	4.62	120.94	0.28	120.52	0.09	x	MSWD = 0.8
z5	123.46	2.79	120.61	0.20	120.47	0.08	x	pof = 0.48
z6	123.11	2.59	119.98	0.19	119.82	0.09		n = 4
19MC-048								
z7	101.71	5.15	102.76	0.25	102.80	0.08		$^{206}Pb/^{238}U$ ± random (+tracer) [+decay constant]
z2	99.87	3.39	102.65	0.19	102.77	0.08		**102.54** **± 0.04** (0.06) [0.13]
z6	103.46	2.33	102.70	0.15	102.67	0.07		
z3b	103.04	2.27	102.57	0.15	102.55	0.07	x	MSWD = 0.5
z3a	104.85	1.83	102.65	0.13	102.55	0.07	x	pof = 0.71
z5	105.57	1.68	102.68	0.13	102.55	0.08	x	n = 4
z4	109.98	1.51	102.81	0.13	102.50	0.07	x	
19MC-052								
z2	104.67	1.62	101.57	0.13	101.44	0.07		$^{206}Pb/^{238}U$ ± random (+tracer) [+decay constant]
z4	104.29	2.79	101.54	0.17	101.42	0.07		**101.18** **± 0.04** (0.06) [0.13]
z5	106.64	1.58	101.56	0.13	101.34	0.07		
z1a	103.37	1.66	101.39	0.13	101.31	0.07		MSWD = 0.5
z1b	103.99	1.65	101.32	0.13	101.20	0.07	x	pof = 0.60
z6	103.12	2.01	101.26	0.14	101.18	0.07	x	n = 3
z3	102.30	1.66	101.20	0.13	101.15	0.07	x	
19MC054								
z6	114.28	2.30	110.62	0.16	110.45	0.08	x	$^{206}Pb/^{238}U$ ± random (+tracer) [+decay constant]
z4	114.43	2.08	110.55	0.15	110.37	0.08	x	**110.36** **± 0.03** (0.06) [0.13]
z5	115.09	2.71	110.56	0.18	110.35	0.08	x	
z3	109.46	4.48	110.30	0.25	110.34	0.08	x	MSWD = 1.4
z2	112.65	2.50	110.44	0.17	110.34	0.08	x	pof = 0.22
z1	113.34	1.79	110.46	0.14	110.33	0.08	x	n = 6

Twenty zircon grains from 19MC-054, leucogranite from the Wolf pluton, yield LA-ICPMS dates between 121 ± 4 and 105 ± 2 Ma. Fifteen dates yield a weighted mean of 109 ± 1 Ma (MSWD = 1.2, pof = 0.22). Six grains were analyzed by CA-TIMS and yield a weighted mean date of 110.36 ± 0.03 / 0.06 / 0.13 Ma (MSWD = 1.4, pof = 0.22; Fig. 3b). This is the interpreted igneous crystallization age.

Seventeen zircon grains from 19MC-048, coarse-grained granite from the Seagull batholith, yield LA-ICPMS dates between 106 ± 3 and 100 ± 2 Ma. All dates yield a weighted mean of 103 ± 1 Ma (MSWD = 1.5, pof = 0.10). Six grains were analyzed by CA-TIMS, with two fragments from one grain being analyzed separately. The four youngest dates yield a weighted mean of 102.54 ± 0.04 / 0.06 / 0.13 Ma (MSWD = 0.5, pof = 0.71; Fig. 3c). This is the interpreted igneous crystallization age. Three grains with dates of 102.80 ± 0.08 to 102.67 ± 0.07 Ma are interpreted as containing inherited components.

Twenty-four zircon grains from 19MC-052, coarse-grained granite from the Hake batholith, yield LA-ICPMS

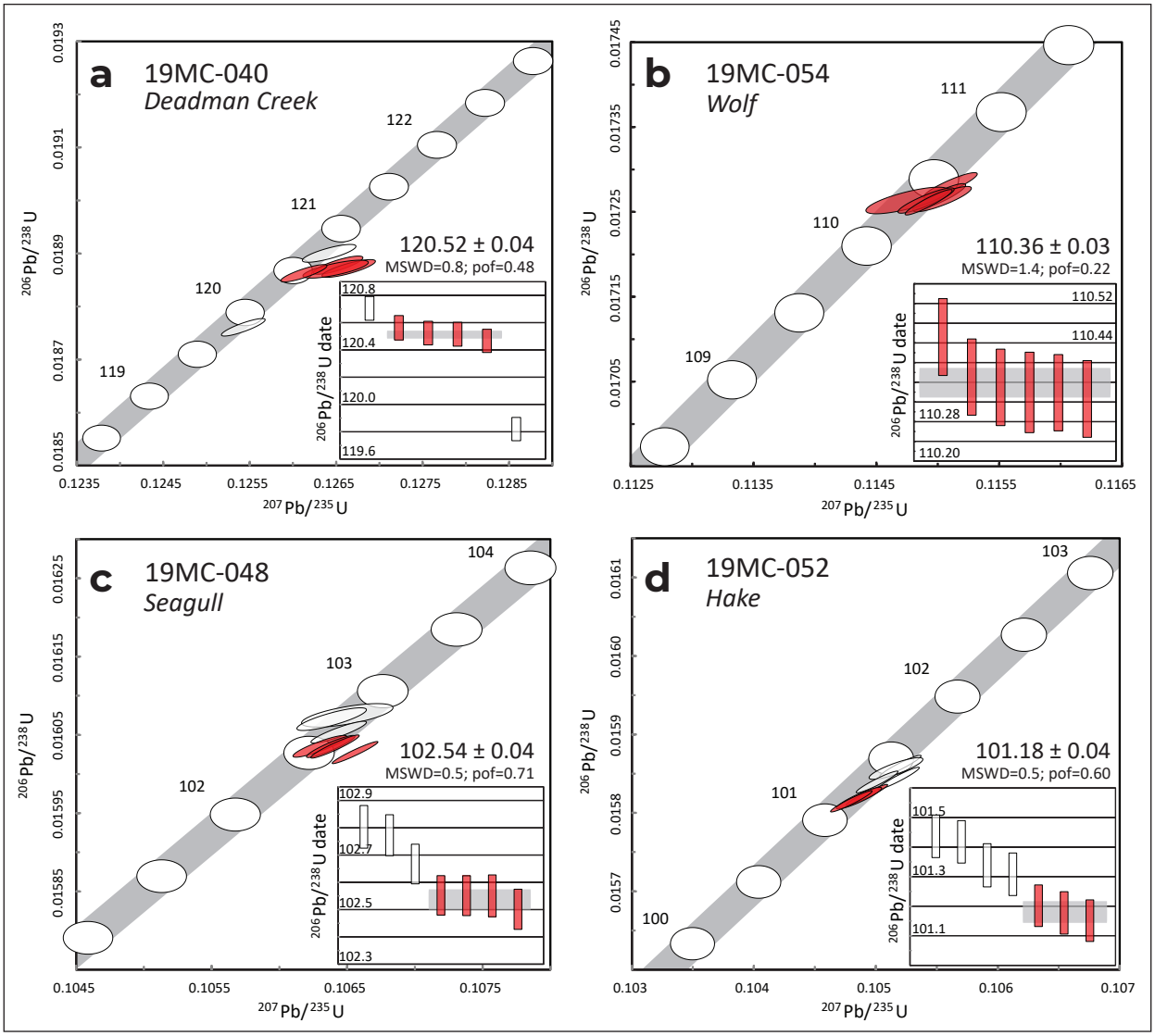

Figure 3. *Concordia diagram and ranked plot of $^{206}U/^{238}Pb$ dates (insets) for zircon analyzed by CA-TIMS (Table 1).* ***(a)*** *Deadman Creek batholith, 19MC-040;* ***(b)*** *Wolf pluton, 19MC-054;* ***(c)*** *Seagull batholith, 19MC-048;* ***(d)*** *Hake batholith, 19MC-052. The concordia curve is shown by the light grey band which includes uncertainties in decay constant. The weighted mean date was calculated with Isoplot 3.0 (Ludwig, 2003) and is represented by grey box behind the error bars on the ranked plot in inset. Analyses used in weighted mean calculation are shown in red. MSWD = Mean Square of Weighted Deviation; pof = probability of fit. All errors are at 2σ.*

dates between 108 ± 3 and 97 ± 5 Ma. Nineteen dates yield a weighted mean of 102 ± 1 Ma (MSWD = 1.2, pof = 0.22). Six grains were analyzed by CA-TIMS, with two fragments from one grain being analyzed separately. The three youngest dates yield a weighted mean of 101.18 ± 0.04 /0.06 / 0.13 Ma (MSWD = 0.5, pof = 0.60; Fig. 3d). This is the interpreted igneous crystallization age. Three grains with dates of 101.44 ± 0.07 to 101.31 ± 0.07 Ma are interpreted as containing inherited components.

Geochemistry

Lithogeochemical analyses were previously published for plutons of the Seagull suite, but <25% of samples were analyzed for the full suite of trace elements (including heat producing elements such as Th and U; Liverton and Alderton, 1994; Liverton *et al.*, 2005; Rasmussen, 2013). No previous geochemical data were published for plutons of the Teslin suite. We collected 6 new samples from the Seagull and Hake batholiths to complement previous data for the Seagull suite, and 9 samples from the Deadman Creek, Wolf and Strawberry Creek plutons to fill the gap for the Teslin suite (Table 2). Samples collected for this study were analyzed by fusion XRF and ICPMS at ALS Global laboratories in Vancouver, B.C. (all data are available online; Yukon Geological Survey, 2020a).

Samples from the Seagull suite generally have high SiO_2 contents (>70%, average 75%) and plot in the granite field of the total alkali *vs.* silica diagram of Le Bas *et al.* (1986; Fig. 4a). They are relatively sodic, with mostly alkali-calcic to alkalic compositions on the modified alkali-lime index (MALI) diagram (Fig. 4b), and straddle the peralkaline and peraluminous fields on the alumina saturation index (ASI) diagram (Fig. 4c). Granites of the Seagull suite are ultra-fractionated with strong enrichment in Th, Rb, U, $_{\Sigma}$REE, Li, B, F^- and Cl^-, elevated HREE, and depletion in CaO, MgO, Al_2O_3, Ba, Eu, Ti and P (Fig. 4d; Liverton and Alderton, 1994; Liverton *et al.*, 2005; Rasmussen, 2013; Liverton, 2016; Yukon Geological Survey, 2020a). Their Rb/Sr ratios are >2 (and up to ~9500) and $^{87}Sr/^{86}Sr_{100}$ range from 0.706 to 0.708 (Liverton and Alderton, 1994; Rasmussen, 2013). They have all the characteristics of A-type granites (Fig. 4e–f). The strongly fractionated granites of the Seagull suite stand as the most evolved plutons in the northern Cordillera (Rasmussen, 2013).

Samples from the Teslin suite have SiO_2 ranging from 58 to 77% (average 68%; Fig. 4a) and major and trace element compositions more typical of peraluminous, calc-alkaline granitoid rocks (Fig. 4b–f; Yukon Geological Survey, 2020a).

Potential Heat Generation

The decay of radioactive elements converts mass into radiation energy, which is an exothermic reaction that produces heat. While all naturally radioactive isotopes can generate some heat, significant heat production only occurs from the decay of ^{238}U, ^{235}U, ^{232}Th and ^{40}K. Therefore, potential heat production is governed by the concentrations of U, Th and K in the rock (Rybach, 1981). In igneous rocks, radiogenic heat production is dependent on the bulk chemistry of the rock and decreases from acidic (*e.g.*, granite) through basic to ultrabasic rock types (Rybach, 1981; Rybach and Buntebarth, 1982, 1984; Hasterok and Webb, 2017). Thus, granites with anomalously high concentrations of U, Th and K, such as plutons of the Seagull suite, are prime targets for calculating potential radiogenic heat production (*A*) using the equation of Rybach (1981):

$$A\ (\mu W/m^3) = \rho\ (9.52cU + 2.56cK + 3.48cTh) \times 10^{-5}$$

where *c* is the concentration of U and Th in ppm, and K in %; and ρ is the rock density (in g/cm^3). Heat production constants of the natural radio-elements U, Th, K are 9.525×10^{-5}, 2.561×10^{-5} and 3.477×10^{-9} W/kg, respectively (Rybach, 1981). Global averages for heat production (*A*) in typical granites range from 2.5 to 2.8 μW/m^3 (Hasterok and Webb, 2017).

The heat production calculations (*A*) for granites of the Seagull suite range between 0.3 and 22.9 μW/m^3, with an average of 6.7 μW/m^3 (n = 70) (Fig. 5; Appendix 4; Friend and Colpron, 2017; Colpron, 2019). More than 50% of the samples yielded *A* values >6.0 μW/m^3 with an average of 9.1 μW/m^3. Of these samples, only 15 were analyzed for all three radiogenic elements (Th, U and K), indicating that estimates of radiogenic

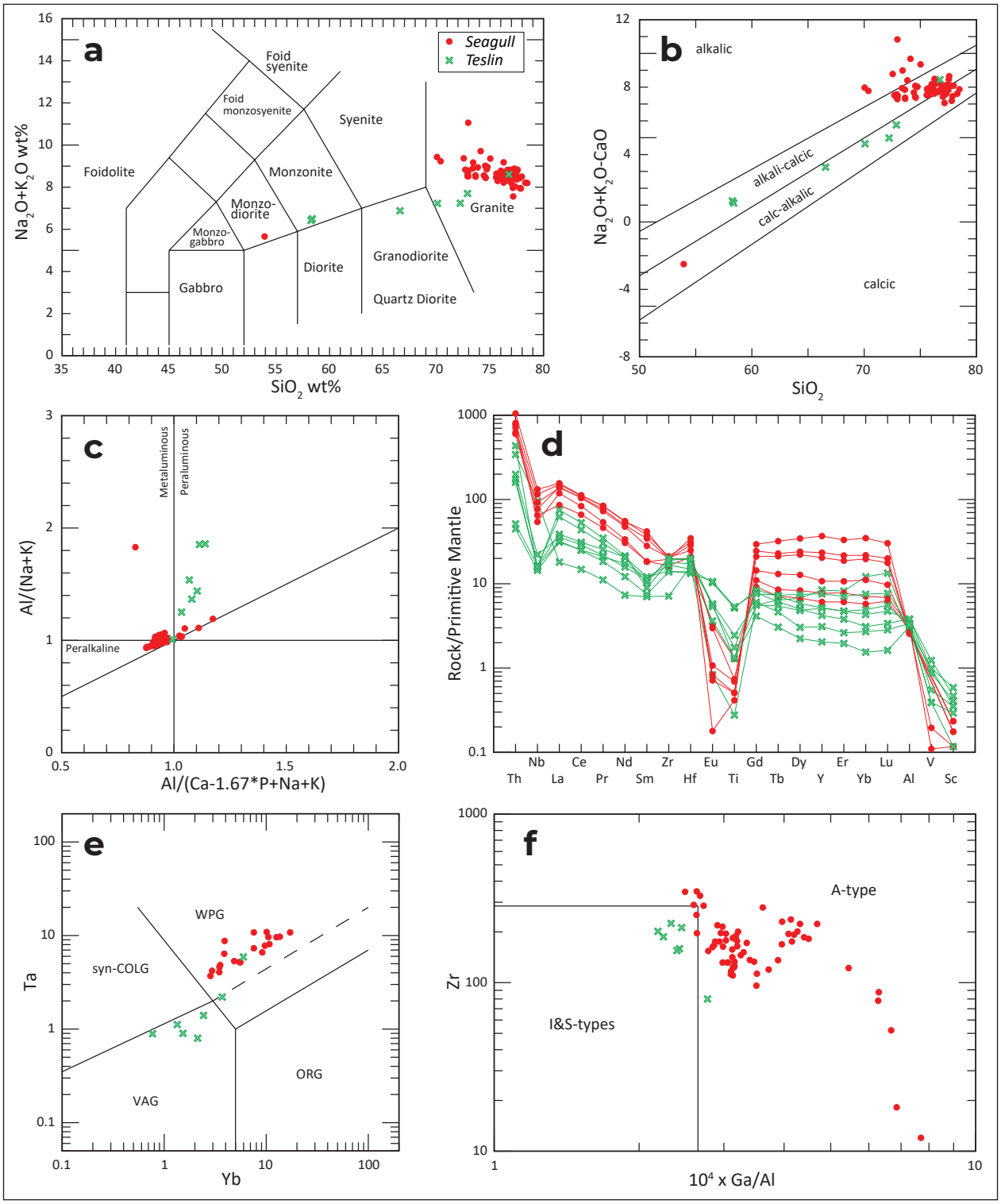

Figure 4. *Geochemical discriminant diagrams for the Seagull and Teslin plutonic suites.* **(a)** *Total alkali vs. SiO_2 diagram of Le Bas et al. (1986).* **(b)** *MALI diagram.* **(c)** *ASI diagram of Shand (1943).* **(d)** *Primitive mantle normalized trace element plot; normalization values of Sun and McDonough (1989).* **(e)** *Ta vs. Yb diagram of Pearce et al. (1984). ORG = ocean ridge granite; syn-COLG = syn-collisional granite; VAG = volcanic arc granite; WPG = within-plate (A-type) granite.* **(f)** *Zr vs. $10^4 \times$ Ga/Al diagram of Whalen et al. (1987).*

heat production are likely minimum values for ≥60% of samples. Seagull suite samples with A >6 μW/m³ generally have cTh >50 ppm (high ~100 ppm) and cU typically >10 ppm (Colpron, 2019; Yukon Geological Survey, 2020a). Samples with A >10 μW/m³ all have cU >20 ppm (high of 58 ppm).

Plutons of the Teslin suite have a wider range of compositions, from mafic to felsic (Fig. 4a), and generally yield heat production values that are closer to global averages, with A values being mostly between 0.9 and 3.1 μW/m³ and averaging 2.0 μW/m³ (Fig. 5; Appendix 4; Colpron, 2019). Two samples from the northern part of the Deadman Creek batholith (near Johnson's Crossing; not shown in Fig. 5) have more felsic compositions and A values of 4.5–5.0 μW/m³ (see Colpron, 2019). One sample from the Wolf pluton is strongly anomalous with A = 11.4 μW/m³ (Fig. 5).

For samples where all three radiogenic elements were analyzed, a ternary plot of Th-U-K relative to their respective heat production constants show that both Th and U are the main heat producing elements in the Seagull suite granites, with Th being dominant

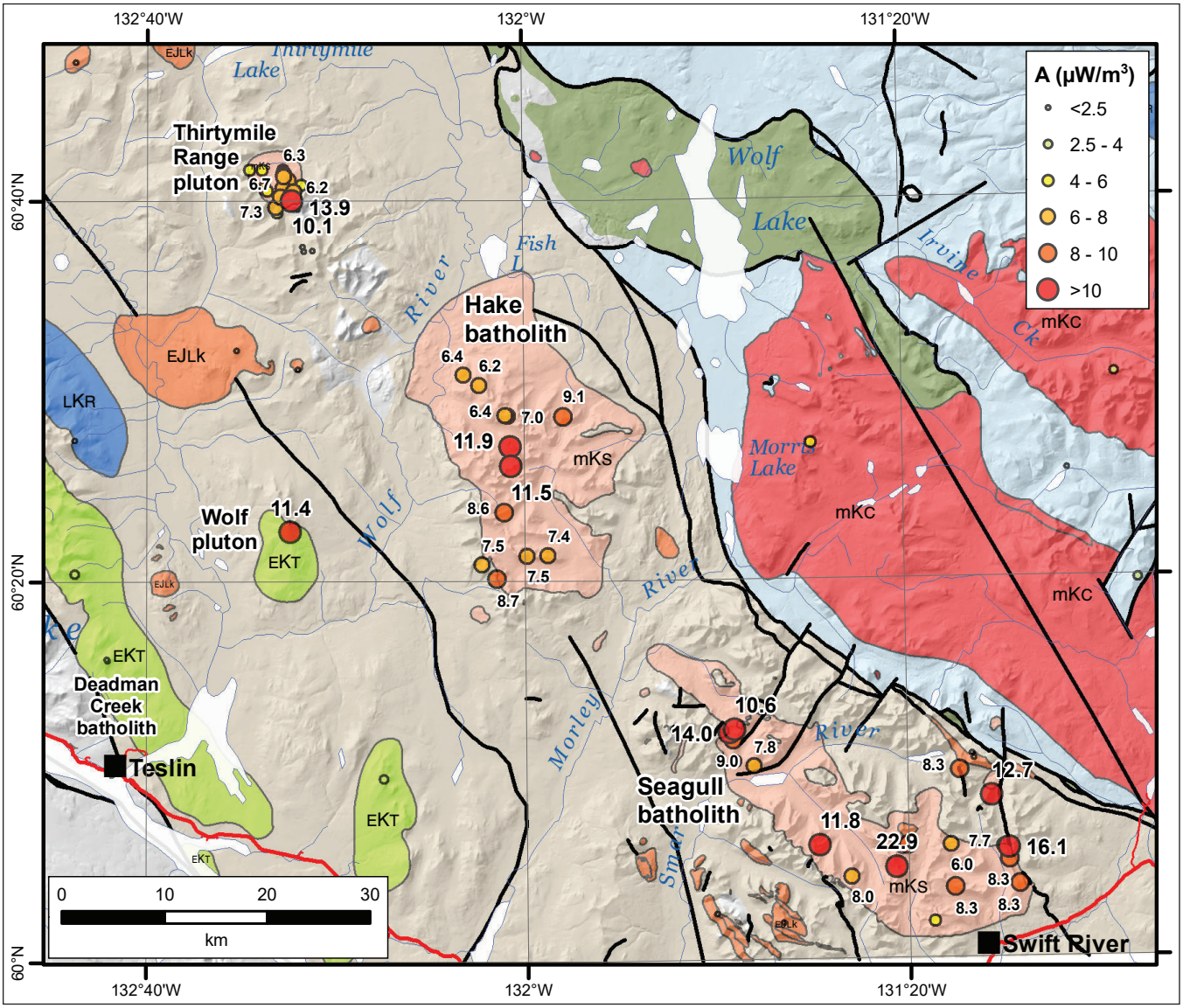

Figure 5. *Potential radiogenic heat production (A) from Mesozoic granitoids in the Teslin–Wolf Lake area of southern Yukon (after Friend and Colpron, 2017; Colpron, 2019). Heat production values were calculated using the equation of Rybach (1981). Lithogeochemical data are from the compilation by the Yukon Geological Survey (2020a). Only samples with A values >6 μW/m³ are labelled; complete list of values are given in Appendix 4 and Colpron (2019).*

in most samples (Fig. 6). The K contribution to heat production in granites of the Seagull suite is negligible. For all Cretaceous plutons, K_2O ranges from 2.5 to 6%, with most samples in the Seagull suite between 4.8 and 5.3% (average of 4.96%), and 2.6 and 3.9% for the Teslin suite (average of 3.19%; Appendix 4). In the Teslin suite, the generally low concentrations in Th (<17 ppm) and U (<5.7 ppm) in most samples result in proportionally more significant K contributions to heat production, although most samples have low to average A values (Fig. 5; Appendix 4). The few samples with anomalous A values all have cTh >29 ppm; the sample from the Wolf pluton, with A = 11.4 μW/m³, has cU = 33.2 ppm (Fig. 6; Appendix 4).

In both the Seagull and Hake batholiths, all samples are anomalous relative to global averages of heat production, with A ranging from 4.4 to 22.9 μW/m³, and >85% of samples have A values >6 μW/m³ (Fig. 5). The average A values for the Hake and Seagull batholiths are 7.9 and 9.9 μW/m³, respectively. Many of the samples with A <10 μW/m³ are lacking analyses for uranium (Colpron, 2019; Yukon Geological Survey, 2020a), suggesting that, although heat production seems primarily driven by cTh, the combination of anomalous Th and U concentrations yields the highest radiogenic heat production potential.

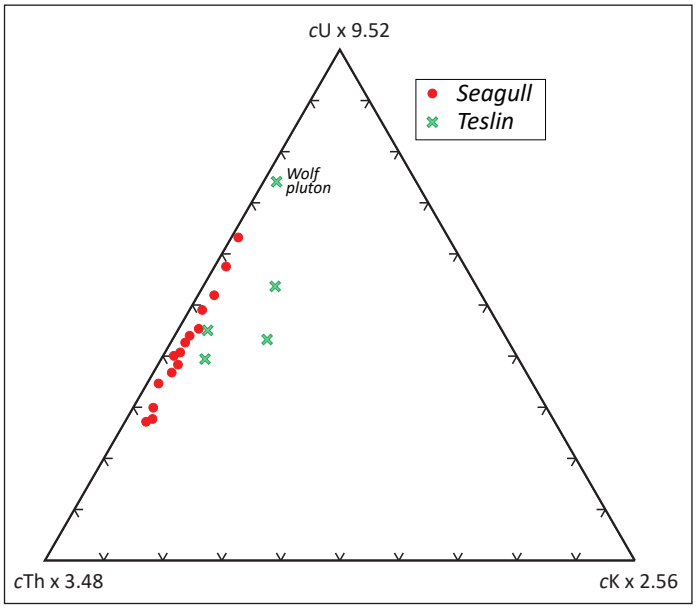

Figure 6. *Ternary Th-U-K diagram illustrating relative contributions to potential heat production calculations.*

A radiometric survey of the Seagull batholith acquired by UCore Rare Minerals Inc. in 2014 (Fig. 7; Kalkowski et *al.*, 2015) provides a means of evaluating the overall Th and U enrichments in this pluton. Figure 7 illustrates that Th enrichment is widespread in the Seagull batholith, whereas U is more concentrated in the southeastern part of the batholith. Samples with A >10 μW/m³ generally correspond with coincident Th and U anomalies. The radiometric survey for the Seagull batholith shows that coincident Th and U anomalies are more widespread in the southeastern portion of the pluton, where some of the highest heat production values are measured (up to 16.1 and 22.9 μW/m³; Figs. 5 and 7), and therefore this region is more prospective for potential radiogenic heat production. It is notable that U ± Th anomalies follow the fault at the eastern edge of the Seagull batholith, and that some of the highest heat production values occur along this same trend (Fig. 7).

Gravity Modeling

Bouguer gravity data for a broad area centered on the Hake and Seagull batholiths (Fig. 8) were gridded at 2 km from data acquired from the Geophysical Data Repository (Geological Survey of Canada, 2019). The data are reduced using a standard crustal Bouguer density of 2670 kg/m³. The Canadian Geodetic Survey and Geological Survey of Canada acquired the regional gravity data (Geological Survey of Canada, 2019) between 1944 and 2015 at a nominal station spacing of ~10 km. All data are tied to the International Gravity Standardization Network 1971 (IGSN 71; Morelli, 1974).

The three-dimensional geometry and character of low-density sources associated with intrusive rocks were investigated through the 3D inversion of Bouguer anomaly data, using the GRAV3D software package (Li and Oldenburg, 1998). The inverse problem is solved by minimizing the data misfit between the observed and predicted anomaly subject to model constraints; a trade-off parameter was used to balance the data fit and model smoothness.

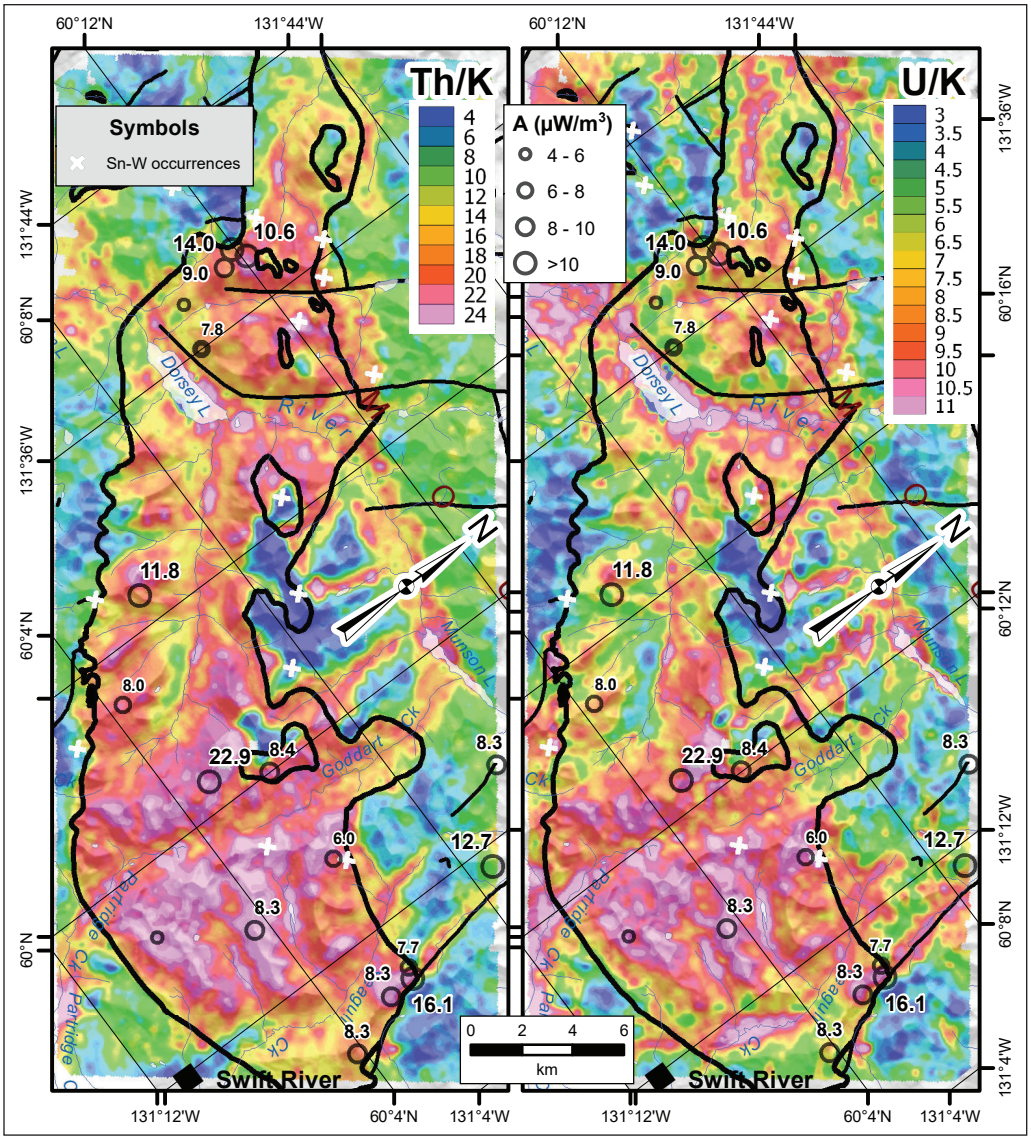

Figure 7. *Airborne radiometric survey results for the Seagull batholith (after Kalkowski et al., 2015).* ***(a)*** *Th/K map.* ***(b)*** *U/K map. Heat production values are from Appendix 4 and Colpron (2019). Note that all values in the Seagull batholith have A >4 μW/m³. Also note that the geographic frame is rotated with North pointing to the upper right.*

The input gravity data were sampled at original survey locations (2854 stations) from the 2 km grids. Model testing determined that upward continuation of the Bouguer data by 5 km was required to minimize model artefacts resulting from shallow-sourced perturbations and noise (Fig. 9a). In order to focus the inversions on the gravitational field associated with local sources, the regional field was removed by subtracting the long-wavelength component of the Bouguer anomaly following its upward continuation to 50 km (Fig. 9b). Surface topography was defined by a grid sampled from ETOPO1 (Amante and Eakins, 2009).

A mesh with a core cell size of $2 \times 2 \times 1$ km was determined from numerous test models to be a good compromise between model smoothness, size, and artefacts. The borders and base of the mesh were padded by increasingly larger cells to a distance/depth of 70/1000 km, respectively, to limit artefacts at model edges. As the inversions are focused on the gravity effects of low-density sources, only negative density contrasts were permitted. Specific gravity data measured from samples collected in the Hake and Seagull batholiths (Table 2) were used to define density constraints during modeling.

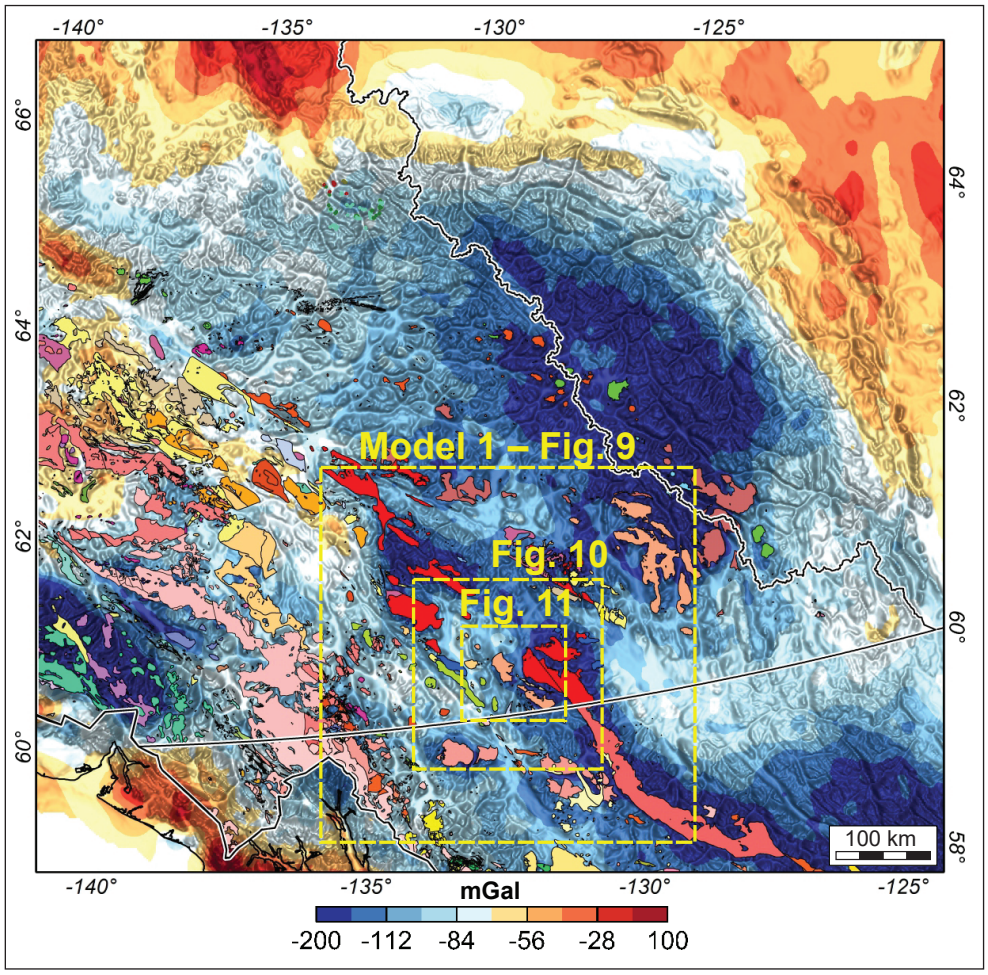

Figure 8. *Bouguer gravity of southern Yukon and surrounds overlain by topography. Coloured polygons show the distribution of mapped intrusive rocks (Cui et al., 2013; Yukon Geological Survey, 2020b). Yellow dashed box shows the locations of models presented below.*

A suite of three models was constructed for the intrusions, based on their combined rock physical property density ranges. The inversions were guided by a reference model with a negative density contrast equal to the higher value of sample density range, and the model bounded to only permit density contrast within the lower limit of the density range (Table 2). For example, the batholiths were initially modeled (Figs. 10 and 11a) with a range of -124 kg/m^3 (lower model bounds) to -58 kg/m^3 (reference density) corresponding to the range of rock physical property data (2546 to 2612 kg/m^3 relative to the Bouguer density of 2670 kg/m^3). The predicted model provided a good fit to the observed gravity with a RMS error of 1.02 mGal. Subsequent models were calculated for the density contrast ranges expanded by ± 10 (Fig. 11b; -134 to -48 kg/m^3) and ± 20 kg/m^3 (Fig. 11c; -144 to -38 kg/m^3), to assess the impact on the models should the intrusions have a wider range of density than constrained by rock physical properties.

The pattern of low-density zones in the models (e.g., Fig. 10) primarily reflect the distribution of relatively lower density intrusive rocks (Figs. 1 and 8). Models (Fig. 11) show low density sources associated with the Hake batholith and Thirtymile Range pluton, despite their limited surface extent and sparsity of gravity observations (Fig. 9a). The surface extent of the Hake batholith is well represented by the model

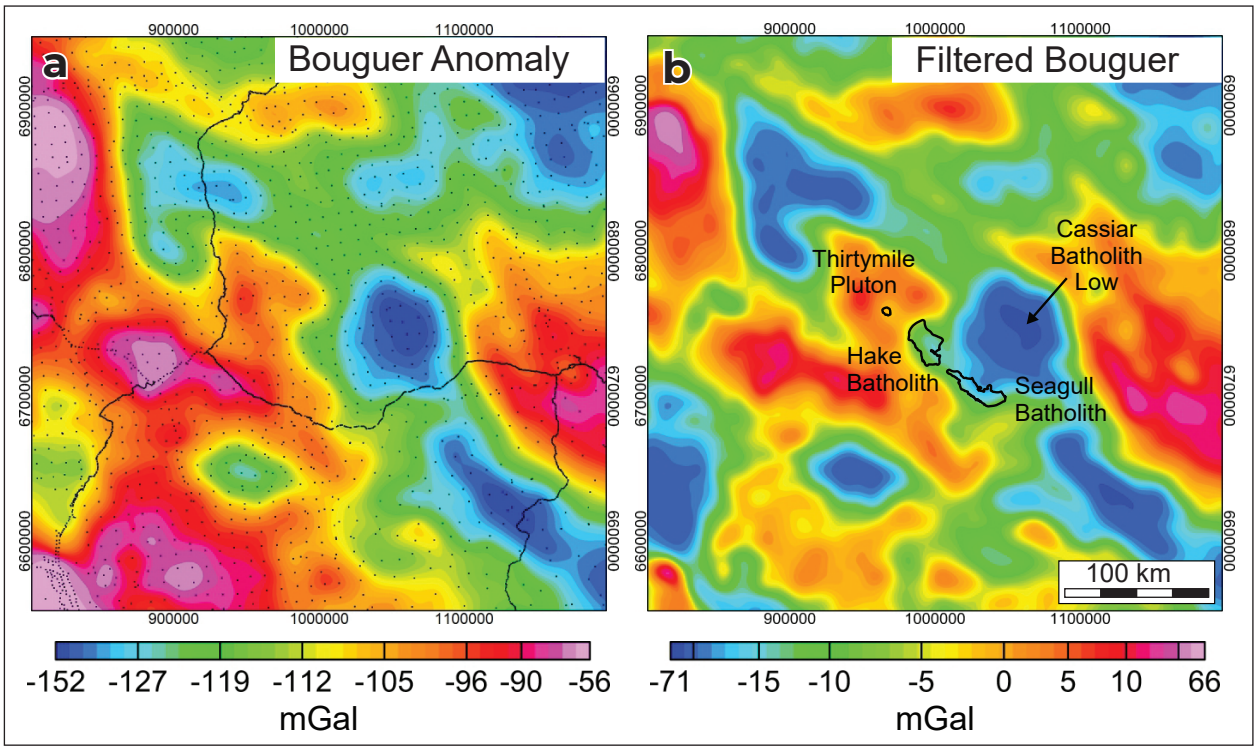

Figure 9. ***(a)*** *Bouguer anomaly, upward continued by 5 km, of the model area. Black dots show gravity station locations, more concentrated along roads.* ***(b)*** *Bouguer anomaly of the model area following removal of the regional field (Bouguer anomaly upward continued to 50 km). Black polygons show the mapped location of the Hake and Seagull batholiths, and Thirtymile pluton (Yukon Geological Survey, 2020b).*

(Fig. 11a), constrained by the rock physical properties in the range of -124 to -58 kg/m^3, but as with the Thirtymile Range pluton, the model may suggest a slightly greater lateral extent for the intrusion at depth. The volume of the Hake batholith is estimated at ~4624 km^3 with a maximum depth of ~11 km (Table 3). For an expanded density range (-134 to -48 kg/m^3), the lateral extent of the intrusion (Fig. 11b) is only slightly increased along with its depth and volume (Table 3). However, for a density range of -144 to -38 kg/m^3, the modeled intrusion (Fig. 11c) greatly exceeds its mapped expression and its estimated volume and depth are significantly greater.

For the Seagull batholith, the -124 to -58 kg/m^3 model (Fig. 11a) shows a source of similar lateral extent, but that is slightly displaced towards the northeast of its mapped expression. Its volume is estimated at ~2744 km^3 with a maximum depth of ~9 km. Increasing the density range (-134 to -48 kg/m^3 and -144 to -38 kg/m^3) results in predicted sources (Fig. 11b,c) that exceed the scale of the mapped expression. Estimates of volume and depth increase steadily in accordance (Table 3).

Discussion

Ultra-fractionated, A-type granites of the Seagull suite (Fig. 4) have heat production values (A) that are between 2 and 6 times higher than global averages (2.5–2.8 µW/m^3; Rybach, 1981; Hasterok and Webb, 2017), despite the fact that more than 60% of samples were not analyzed for a full suite of heat producing elements (Fig. 5; Appendix 4; Friend and Colpron, 2017; Colpron, 2019). The 6 samples collected from the Hake and Seagull batholiths for this study were analyzed for a full suite of trace elements and yielded A values ranging from 8.3 to 22.9 µW/m^3 (Fig. 5; Colpron, 2019; Yukon Geological Survey, 2020a), suggesting that for samples with incomplete analyses, heat production

Table 2. *Sample descriptions, locations and rock physical property data.*

Sample [1]	Latitude	Longitude	Lithology	Pluton	Magnetic susceptibility (10^{-3} SI units)[2]	Density (kg/m³)[3]	Density range (relative to Bouguer density of 2670 kg/m³)
Teslin plutonic suite							
19MC-036	60.161219	-132.248483	Medium-grained, equigranular Bt granite	Strawberry Creek pluton	3.52	2622	-48 to -62
19MC-037	60.160259	-132.249158	Coarse-grained, equigranular Bt granite	Strawberry Creek pluton	2.31	2608	
19MC-038	60.264854	-132.733467	Fine-grained Bt-Hbl diorite	Deadman Creek batholith	0.235	2713	-131 to -69
19MC-039	60.265657	-132.734871	Fine-grained Bt-Hbl diorite	Deadman Creek batholith		2711	
19MC-040	60.340521	-132.792034	Foliated, K-feldspar porphyritic Bt-Hbl granodiorite	Deadman Creek batholith	0.2	2680	
19MC-042	60.440648	-132.85519	Foliated, K-feldspar porphyritic Bt granodiorite	Deadman Creek batholith	0.204	2605	
19MC-043	60.509529	-133.036268	Medium-grained, equigranular Hbl-Bt granodiorite	Deadman Creek batholith	4.27	2601	
19MC-044	60.508212	-133.030736	Fine-grained Hbl diorite	Deadman Creek batholith	25	2801	
19MC-046	60.587557	-133.211117	Very coarse grained, equigranular, Bt-Hbl granodiorite	Deadman Creek batholith	2.85	2634	
19MC-054	60.377727	-132.412548	Medium-grained, equigranular leucogranite	Wolf pluton	0.0618	2573	-97
Seagull plutonic suite							
19MC-047	60.064369	-131.139421	Coarse-grained, equigranular, Bt granite	Seagull batholith	0.0207	2562	-78 to -124
19MC-048	60.062013	-131.251974	Coarse-grained, equigranular, Bt granite	Seagull batholith	0.0292	2592	
19MC-049	60.080551	-131.353948	Fine-grained, equigranular, Bt granite	Seagull batholith	0.058	2586	
19MC-050	60.100482	-131.487644	Coarse-grained, K-feldspar porphyritic Bt granite	Seagull batholith	0.212	2546	
19MC-052	60.394268	-132.034807	Coarse-grained Bt granite with partilally developed rapakivi texture	Hake batholith	1.04	2612	-58 to -84
19MC-053	60.477356	-131.930008	Coarse-grained, K-feldspar porphyritic Bt granite	Hake batholith	0.64	2586	

Notes:

[1] Samples shown in **Bold** were selected for geochronology

[2] Magnetic susceptibility is average of 5 or more measurements on the outcrop using a SM-30

[3] Density was measured from hand sample in the Yukon Geological Survey laboratory

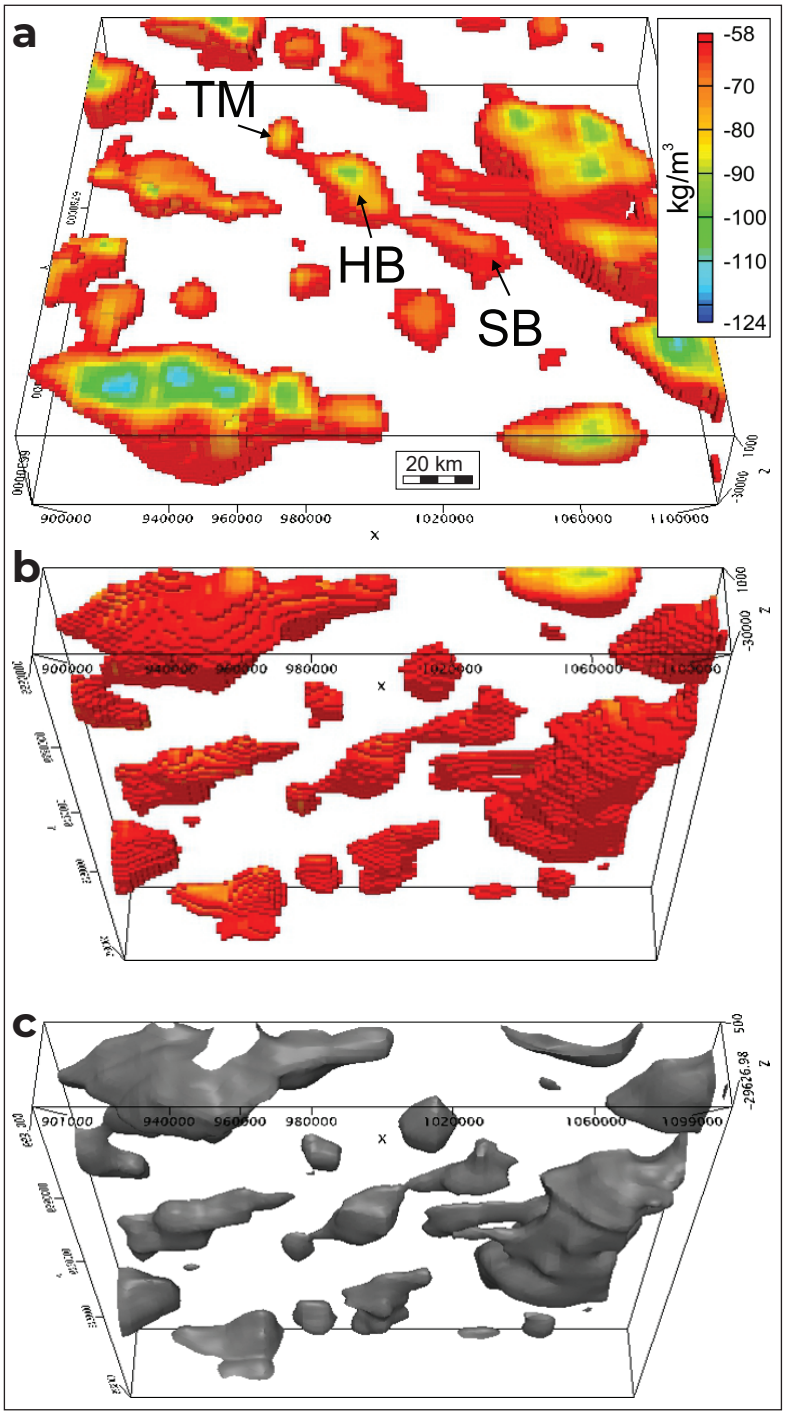

Figure 10. *3D Perspective views of the model density results from the Hake and Seagull batholiths for a density contrast range of -124 to -58 kg/m³.* **(a)** *View from above.* **(b)** *View from below* **(c)** *-58 kg/m³ isosurface viewed from below. See Figure 8 for location.*

values are likely underestimated by 30–60%; the relative contribution of cU in samples plotted in Figure 6. A radiometric survey of the Seagull batholith shows that although the whole batholith is highly radiogenic, the southeastern portion of the pluton near Swift River is likely more prospective for radiogenic heat production as coincident Th and U anomalies are more extensive in this region (Fig. 7).

Plutons of the Teslin suite have generally more intermediate compositions (Fig. 4) and A values that are equal to, or lower than, global averages (Fig. 5; Appendix 4; Colpron, 2019; Yukon Geological Survey, 2020a). Anomalous A values occur in more evolved granite phases of the Deadman Creek batholith (4.5–5.0 μW/m³; Colpron, 2019) and in one sample from the Wolf pluton, which has cU of 33.2 ppm resulting in A = 11.4 μW/m³ (Figs. 5 and 6; Yukon Geological Survey, 2020a). More detailed mapping of evolved granodiorite to granite phases in the Deadman Creek batholith would assist in identifying parts of the batholith more prospective for radiogenic heat production.

The new U-Pb zircon CA-TIMS dates for plutons of the Teslin and Seagull suites provide more precise age constraints that are generally in agreement with previously published dates (Fig. 1; Gordey *et al.*, 1998; Mortensen *et al.*, 2006, 2007). The older, foliated and lineated diorite to granodiorite phase of the Deadman Creek batholith is dated at *ca.* 121 Ma, whereas more evolved, post-tectonic granites in the Deadman Creek, Wolf and Strawberry Creek plutons yielded dates of *ca.* 110–108 Ma (Figs. 1 and 3). If local deformation in the Deadman Creek batholith is related to displacement along part of the Teslin fault system, then deformation along this segment of the fault had ceased by *ca.* 110 Ma. However, other segments of the fault may have been active into the Paleocene (Mihalynuk *et al.*, 2006).

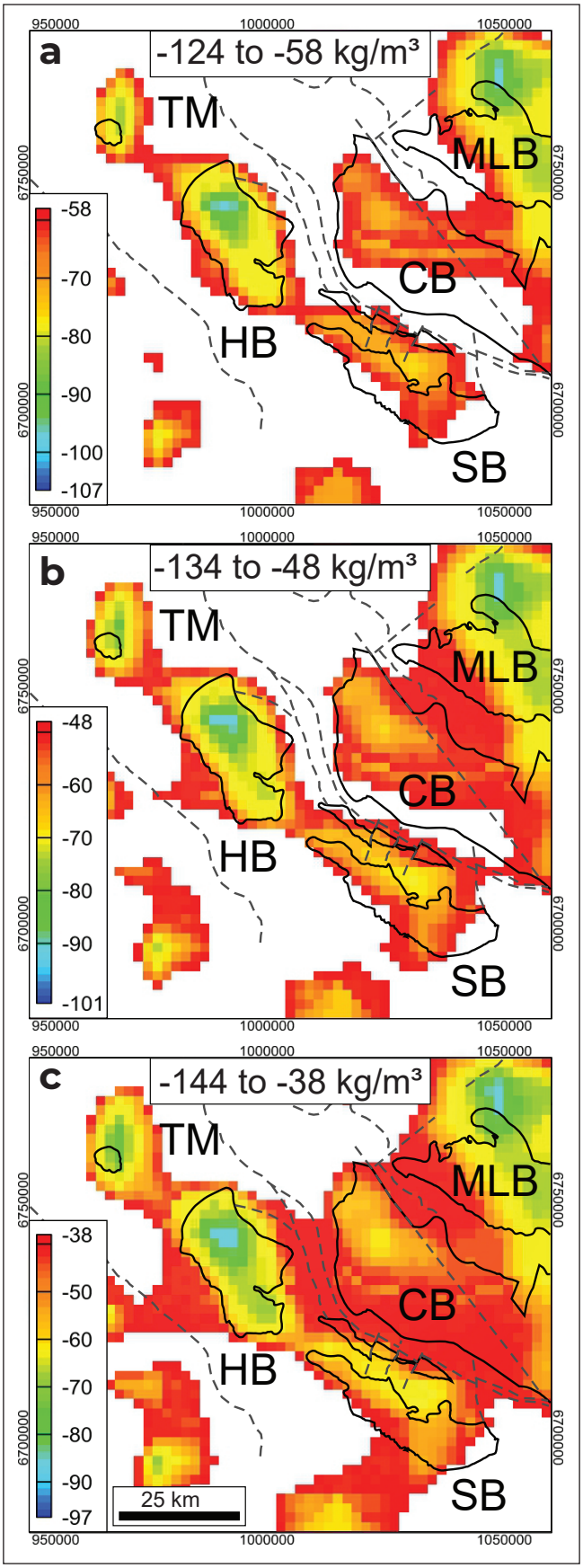

Granites of the Seagull suite are distinctly younger than the Teslin suite, with dates of *ca.* 103–101 Ma for the Thirtymile Range, Hake and Seagull plutons (Figs. 1 and 3). Previous LA-ICPMS dates from the northern part of the Seagull batholith are somewhat younger at 99–96 Ma (Mortensen *et al.*, 2006); this part of the batholith was not redated in this study using the more precise CA-TIMS method.

Gravity inversion model results that are based on measured rock physical properties (density contrast of -124 to -58 kg/m^3; Table 2) provide a good estimate for the extents of the Hake and Seagull batholiths (Table 3). Models for the Hake batholith are closely concordant with its mapped expression (Fig. 11). The volume of the pluton is estimated at ~4624 km^3 with a maximum depth of ~11 km (Table 3). The Seagull batholith is smaller with an estimated volume of ~2744 km^3 and a maximum depth of ~9 km (Table 3), but its modeled source is displaced to the northeast relative to its mapped expression (Fig. 11).

The apparent northeast displacement of the source associated with the Seagull batholith may indicate that the batholith dips towards the northeast and/or that the sparsely sampled gravity data are inadequate to accurately model the small intrusion. The majority of rocks adjacent to the pluton include typically higher density rocks of the Snowcap and Finlayson assemblages of the Yukon-Tanana terrane (Enkin, 2018; Yukon Geological Survey, 2020b). However, the Cassiar batholith (Fig. 11), which is associated with a large gravity low northeast of the Seagull batholith (Fig. 9), may be partly responsible for displacing the low-density source in the inversion results. Similarly, the location and scale of the small Thirtymile Range pluton are not well-defined by model results (Figs. 10 and 11), suggesting that smaller plutons may not be well constrained by the low spatial density of the

Figure 11. *Model density results for the Hake and Seagull batholiths, and Thirtymile Range pluton. Simplified geology from Yukon Geological Survey (2020b).*
(a) *Model density constraints -124 to -58 kg/m^3.*
(b) *Model density constraints -134 to -48 kg/m^3.*
(c) *Model density constraints -144 to -38 kg/m^3. Batholiths and plutons: TM = Thirtymile, HB = Hake, SB = Seagull, MLB = Marker Lake, CB = Cassiar.*

Table 3. *Estimated batholith volumes and maximum depths (below sea level) from density models using different reference densities.*

Range in Density Contrast (kg/m^3)	Density Range adjusted for Bouguer density (2670 kg/m^3)	Volume (km^3)	Max Depth (km)	Average A (μW/m^3)	Potential Heat Energy (MWt)
Hake batholith					
-124 to -58	2546 to 2612	4624	11	7.9	36.5
-134 to -48	2536 to 2622	6464	13	7.9	51.1
-144 to -38	2526 to 2632	11112	15	7.9	87.8
Seagull batholith					
-124 to -58	2546 to 2612	2744	9	9.9	27.2
-134 to -48	2536 to 2622	4928	13	9.9	48.8
-144 to -38	2526 to 2632	11612	18	9.9	115.0

gravity observations. Model resolution and accuracy would be improved with the acquisition of a denser grid of gravity data.

Both the Hake and Thirtymile Range plutons appear to have slightly larger extents at depth, but all plutons of the Seagull suite are relatively shallow with maximum depths of 9–11 km (Fig. 10; Table 3). The inversion model results may support the idea that these bodies are connected at depth (Liverton *et al.*, 2005), but the resolution of the input gravity data are not sufficient to be definitive and the relatively shallow maximum depths for these plutons limit the potential size of a regional batholith.

Using the volumes estimated by 3D inversion of regional Bouguer gravity data and average radiogenic heat production values, the Hake and Seagull batholiths contain potential heat energy of approximately 36.5 and 27.2 MWt, respectively (Table 3). When added to the elevated heat flow documented in the northern Cordillera (~105 ± 22 mW/m^2; Lewis *et al.*, 2003), the relatively thin crustal thickness (~32–35 km) and the shallow Curie point depths in the Teslin region (Witter and Miller, 2017; Witter *et al.*, 2018), these radiogenic heat sources could locally amplify near surface temperature gradients.

Lachenbruch (1970) has shown that shallow crustal heat flow and heat production in plutonic rocks have a near linear relationships such that:

$$q = 27 + 16.6A$$

where q is heat flow in mW/m^2 and A is the heat production in μW/m^3 (Beamish and Busby, 2016). This linear relationship shows little variation between differing crustal provinces (Lachenbruch, 1970; Hyndman and Lewis, 1999), and in the northern Cordillera Lewis *et al.* (2003) measured an average heat production (A) of 4.6 ± 2.4 μW/m^3, which corresponds to heat flow (q) of ~103 mW/m^2 within range of measured average heat flow of 105 ± 22 mW/m^2. When we apply Lachenbruch's (1970) equation to average heat production values for the Hake and Seagull batholiths, heat flow values of 158–191 mW/m^2 are suggested; these values are 50–80% above the regional average for the northern Cordillera (Lewis *et al.*, 2003).

Part of this energy could be harnessed if deep aquifers were heated and circulated to shallow depths. The granites themselves are likely poor targets for development of a geothermal reservoir, due to their expected poor porosity and permeability, except perhaps along faults (Fig. 1). A potential geothermal reservoir could however be developed in more porous limestone and marble of the Yukon-Tanana terrane mapped along the southern margin of the Seagull

batholith near Swift River (see Roots *et al.*, 2004). This portion of the Seagull batholith is the most radiogenic in the radiometric survey (Fig. 7), but the small modeled extent of the pluton at depth limits potential heating of the country rocks to its immediate margins. Crustal-scale thermal modeling, which is beyond the scope of the present study, is required in order to further evaluate the potential for the radiogenic granites to generate local geothermal anomalies.

The north-striking fault mapped north of Swift River is perhaps the most interesting target for geothermal exploration near the southeastern margin of the Seagull batholith (Fig. 1; Roots *et al.*, 2004). The fault is locally intruded by the Seagull batholith and appears to have provided a conduit during pluton emplacement, as suggested by Th and U anomalies following this structure in the radiometric survey (Fig. 7). A small satellite pluton of the Seagull suite was intruded along the fault to the north and has a heat production value of 12.7 μW/m^3, while samples collected at the eastern margin of the Seagull batholith have *A* ranging from 8.3 to 16.1 μW/m^3 (Fig. 5).

Radiogenic granites of the Cornubian province of SW England present an analogue for a potential geothermal system in plutons of the Seagull suite of southern Yukon (Beamish and Busby, 2016). Cornwall has the highest measured heat flow in England and this is directly related to radiogenic heat productions from the granites. It is the site of the only geothermal development project in the UK, where deep drilling (2500–4500 m) is targeting a permeable fault zone and the hot dry granite provides the heat source for an enhanced geothermal system (United Downs Deep Geothermal Power project; Ledingham *et al.*, 2019). Bottom hole temperatures of ~190°C are expected at United Downs and anticipated electricity generation ranges from 1–3 MWe. The southern Seagull batholith could be suitable for a similar geothermal energy generating system, but it should be noted that heat production values in the Seagull batholith (average of 9.9 μW/m^3) are 2–3 times higher than those measured in the Cornubian batholith (~2.5–5.0 μW/m^3; Beamish and Busby, 2016). This may suggest that temperatures sufficient for electricity generation could occur at shallower depths in the Seagull batholith compared to United Downs in Cornwall.

Conclusions

Ultra-fractionated, A-type granites of the Seagull plutonic suite are dated at *ca.* 103–101 Ma and have some of the highest potential for radiogenic heat production in southern Yukon (average of 9.1 μW/m^3). A radiometric survey of the Seagull batholith shows that heat producing elements are anomalous over large parts of this pluton, with the southeastern sector showing the highest potential for radiogenic heat production. The 3D inversion of regional Bouguer gravity resolves zones of low-density associated with the Seagull suite plutons and provide good density models on a mesh of 2 × 2 × 1 km, despite the relatively large gravity station spacing. Models for the Hake batholith match well its mapped extent and suggest an estimated volume of ~4624 km^3 with a maximum depth of ~11 km. The Seagull batholith is smaller with an estimated volume of ~2744 km^3 and a maximum depth of ~9 km, but its modeled source is displaced to the northeast relative to its mapped expression. Using the volumes estimated by 3D inversion of regional Bouguer gravity data and average radiogenic heat production values, the Hake and Seagull batholiths potentially hold heat energy of ~36.5 and 27.2 MWt, respectively.

Acknowledgements

Tiffani Fraser, Julie Minor, Carolyn Relf and Jeff Witter participated in field work for this study. Melissa Friend was instrumental in initiating the data compilation that led to initial assessment of potential radiogenic heat production in Yukon. Further development of the Yukon lithogeochemical dataset would not have been possible without help from Justin Emberley and Amanda O'Connor. Safe flying to field locations was provided by Capital Helicopters. Specific gravity measurements were obtained at the Yukon Geological Survey's rock property lab by Justin Emberley. Jeff Witter provided comments that helped enhance the paper. Funding for geothermal research at YGS was provided by the Government of Canada Canadian Northern Economic Development Agency's Strategic Initiatives in Northern Economic Development (SINED) Fund and the Government of Yukon. This is Geological Survey of Canada contribution 20200585.

References

Abbott, J.G., 1981. Geology of Seagull tin district. *In:* Yukon Geology and Exploration 1979-80, Indian and Northern Affairs Canada, Exploration and Geological Services Division, p. 32–44.

Amante, C. and Eakins, B.W., 2009. ETOPO1 1 Arc-Minute Global Relief Model: Procedures, Data Sources and Analysis. NOAA Technical Memorandum NESDIS NGDC-24. National Geophysical Data Center, NOAA. doi:10.7289/V5C8276M, [accessed October 2017].

Beamish, D. and Busby, J., 2016. The Cornubian geothermal province: heat production and flow in SW England: estimates from boreholes and airborne gamma-ray measurements. Geothermal Energy, vol. 4, p. 1–25. doi: 10.1186/s40517-016-0046-8.

Colpron, M., 2019. Potential radiogenic heat production from granitoid plutons in Yukon. Yukon Geological Survey, Open File 2019-16.

Colpron, M., Israel, S. and Friend, M., 2016. Yukon plutonic suites. Yukon Geological Survey, Open File 2016-37, 1:750 000 scale.

Condon, D.J., Schoene, B., McLean, N.M., Bowring, S.A. and Parrish, R., 2015. Metrology and traceability of U–Pb isotope dilution geochronology (EARTHTIME Tracer Calibration Part I). Geochimica et Cosmochimica Acta, vol. 164, p. 464–480.

Crowley, J.L., Schoene, B. and Bowring, S.A., 2007. U-Pb dating of zircon in the Bishop Tuff at the millennial scale. Geology, vol. 35, p. 1123–1126.

Cui, Y., Katay, F., Nelson, J. L., Han, T., Desjardins, P. J. and Sinclair L., 2013. British Columbia digital geology. British Columbia Ministry of Energy, Mines and Petroleum Resources, B.C. Geological Survey, Open File 2013-4.

Enkin, R.J. 2018. The Canadian Rock Physical Property Database - First Public Release, Geological Survey of Canada, Open File 8460, 126 p.

Friend, M. and Colpron, M., 2017. Potential radiogenic heat production from Cretaceous and younger granitoid plutons in southern Yukon. Yukon Geological Survey, Open File 2017-60, scale 1:1 000 000.

Gabrielse, H., Murphy, D.C. and Mortensen, J.K., 2006. Cretaceous and Cenozoic dextral orogen-parallel displacements, magmatism and paleogeography, north-central Canadian Cordillera. *In:* Paleogeography of the North American Cordillera: Evidence For and Against Large-Scale Displacements, J.W. Haggart, J.W.H. Monger and R.J. Enkin (eds.), Geological Association of Canada, Special Paper 46, p. 255–276.

Geological Survey of Canada, 2019. Geoscience Data Repository for Geophysical Data, Gravity, Point Data. Natural Resources Canada, http://gdr.agg.nrcan.gc.ca/gdrdap/dap/searcheng.php1, [accessed July 15, 2020].

Gerstenberger, H. and Haase, G., 1997. A highly effective emitter substance for mass spectrometric Pb isotope ratio determinations. Chemical Geology, vol. 136, p. 309–312.

Gordey, S.P., McNicoll, V.J. and Mortensen, J.K., 1998. New U-Pb ages from the Teslin area, southern Yukon, and their bearing on terrane evolution in the northern Cordillera. Geological Survey of Canada, Current Research 1998-F, p. 129–148.

Hasterok, D. and Webb, J., 2017. On the radiogenic heat production of igneous rocks. Geoscience Frontiers, vol. 8, p. 919–940.

Hayward, N., 2019. The 3D Geophysical Investigation of a Middle Cretaceous to Paleocene Regional Décollement in the Cordillera of Northern Canada and Alaska. Tectonics, vol. 38, p. 1–28, https://doi.org/10.1029/2018TC005295.

Hiess, J., Condon, D.J., McLean, N. and Noble, S.R., 2012. $^{238}U/^{235}U$ systematics in terrestrial uranium-bearing minerals. Science, vol. 335, p. 1610–1614.

Hyndman, R.D. and Lewis, T.J., 1999. Geophysical consequences of the Cordillera-Craton thermal transition in southwestern Canada. Tectonophysics, vol. 306, p. 397–422.

Jaffey, A.H., Flynn, K.F., Glendenin, L.E., Bentley, W.C. and Essling, A.M., 1971. Precision measurements of half-lives and specific activities of ^{235}U and ^{238}U. Physical Review C, vol. 4, p. 1889–1906.

Kalkowski, T., Dziuba, F. and Robinson, J., 2015. Staking, soil sampling, prospecting and airborne geophysics report – Seagull tin project. Yukon Energy, Mines and Resources, Assessment Report 096722, 50 p.

Krogh, T.E., 1973. A low contamination method for hydrothermal decomposition of zircon and extraction of U and Pb for isotopic age determination. Geochimica et Cosmochimica Acta, vol. 37, p. 485–494.

Lachenbruch, A.H., 1970. Crustal temperature and heat production: implications of the linear heat-flow relation. Journal of Geophysical Research, vol. 75, p. 3291–3300.

Le Bas, M.J., Le Maitre, R.W., Streckeisen, A. and Zanettin, B., 1986. A chemical classification of volcanic rocks based on the total alkalis-silica diagram. Journal of Petrology, vol. 27, p. 745–750.

Ledingham, P., Cotton, L. and Law, R., 2019. The United Downs Deep Geothermal Power Project. Proceedings, 44th Workshop on Geothermal Reservoir Engineering, Stanford University, California, p. 1–11.

Lewis, T.J., Hyndman, R.D. and Flück, P., 2003. Heat flow, heat generation, and crustal temperatures in the northern Cordillera: Thermal controls of tectonics. Journal of Geophysical Research, vol. 108, p. 2316.

Li, Y. and Oldenburg, D.W., 1998. 3D inversion of gravity data. Geophysics, vol. 63, p. 109–119.

Liverton, T., 2016. A-type granite plutons and tin skarn in southeast Yukon: Mindy prospect and surrounding granites of 105C/9. *In:* Yukon Exploration and Geology 2015, K.E. MacFarlane and M.G. Nordling (eds.), Yukon Geological Survey, p. 151–164.

Liverton, T. and Alderton, D.H.M., 1994. Plutonic rocks of the Thirtymile Range, Dorsey terrane: ultrafractionated tin granites in the Yukon. Canadian Journal of Earth Sciences, vol. 31, p. 1557–1568.

Liverton, T., Mortensen, J.K. and Roots, C.F., 2005. Character and metallogeny of Permian, Jurassic and Cretaceous plutons in the southern Yukon-Tanana terrane. *In:* Yukon Exploration and Geology 2004, D.S. Emond, L.L. Lewis and G.D. Bradshaw (eds.), Yukon Geological Survey, p. 147–165.

Ludwig, K.R., 2003. User's Manual for Isoplot 3.00. Berkeley Geochronology Center, Berkeley, CA, 70 p.

Mattinson, J.M., 2005. Zircon U-Pb chemical abrasion ("CA-TIMS") method: combined annealing and multi-step partial dissolution analysis for improved precision and accuracy of zircon ages. Chemical Geology, vol. 220, p. 47–66.

Mihalynuk, M.G., Friedman, R.M., Devine, F. and Heaman, L.M., 2006. Protolith age and deformation history of the Big Salmon complex, relicts of a Paleozoic continental arc in northern British Columbia. *In:* Paleozoic Evolution and Metallogeny of Pericratonic Terranes at the Ancient Pacific Margin of North America, Canadian and Alaskan Cordillera, M. Colpron and J.L. Nelson (eds.), Geological Association of Canada, Special Paper 45, p. 179–200.

Morelli, C., 1974. The international gravity standardization net 1971. International Association of Geodesy, Special Publication 4, 194 p.

Mortensen, J.K., Brand, A. and Liverton, T., 2007. Laser ablation ICP-MS zircon ages for Cretaceous plutonic rocks in the Logtung and Thirtymile Range areas of southern Yukon. *In:* Yukon Exploration and Geology 2006, D.S. Emond, L.L. Lewis and L.H. Weston (eds.), Yukon Geological Survey, p. 213–221.

Mortensen, J.K., Sluggett, C.L., Liverton, T. and Roots, C.F., 2006. Uranium-lead ID-TIMS and LA-ICP-MS ages for the Cassiar and Seagull batholiths, Wolf Lake map area, southern Yukon. *In:* Yukon Exploration and Geology 2005, D.S. Emond, G.D. Bradshaw, L.L. Lewis and L.H. Weston (eds.), Yukon Geological Survey, p. 257–266.

Pearce, J.A., Harris, N.B.W. and Tindle, A.G., 1984. Trace element discrimination diagrams for the tectonic interpretation of granitic rocks. Journal of Petrology, vol. 25, p. 956–983.

Rasmussen, K.L., 2013. The timing, composition, and petrogenesis of syn- to post-accretionary magmatism in the northern Cordilleran miogeocline, eastern Yukon and southwestern Northwest Territories. Unpublished PhD thesis, University of British Columbia, 788 p.

Roots, C.F., Nelson, J.L. and Stevens, R.A., 2004. Bedrock geology, Seagull Creek (105B/3), southern Yukon (1:50 000 scale). Yukon Geological Survey, Open File 2004-1.

Rybach, L., 1981. Geothermal systems, conductive heat flow, geothermal anomalies. *In:* Geothermal Systems: Principles and Case Histories, L. Rybach and L.J.P. Muffler (eds.), John Wiley & Sons, p. 3–31.

Rybach, L. and Buntebarth, G., 1982. Relationships between the petrophysical properties density, seismic velocities, heat generation, and mineralogical constitution. Earth and Planetary Science Letters, vol. 57, p. 367–376.

Rybach, L. and Buntebarth, G., 1984. The variation of heat generation. density and seismic velocity with rock type in the continental lithosphere. Tectonophysics, vol. 103, p. 335–344.

Sack, P.J., Colpron, M., Crowley, J.L., Ryan, J.J., Allan, M.M., Beranek, L.P., Joyce, N.L., Mortensen, J.K., Israel, S. and Chapman, J.B., 2020. Atlas of Late Triassic to Jurassic plutons in the Intermontane terranes of Yukon. Yukon Geological Survey, Open File 2020-1, 365 p.

Schmitz, M.D. and Schoene, B., 2007. Derivation of isotope ratios, errors and error correlations for U-Pb geochronology using ^{205}Pb-^{235}U-(^{233}U)-spiked isotope dilution thermal ionization mass spectrometric data. Geochemistry, Geophysics, Geosystems (G3), vol. 8, Q08006, doi:10.1029/2006GC001492.

Shand, S.J., 1943. Eruptive Rocks; Their Genesis, Composition, Classification, and Their Relation to Ore Deposits, with a Chapter on Meteorites. Hafner Publishing Co., New York, 444 p.

Sláma, J., Košler, J, Condon, D.J., Crowley, J.L., Gerdes, A., Hanchar, J.M., Horstwood, M.S.A., Morris, G.A., Nasdala, L., Norberg, N., Schaltegger, U., Schoene, B. Tubrett, M.N. and Whitehouse, M.J., 2008. Plešovice zircon — A new natural reference material for U–Pb and Hf isotopic microanalysis. Chemical Geology, vol. 249, p. 1–35.

Sun, S.S. and McDonough, W.F., 1989. Chemical and isotopic systematics of oceanic basalts: implications for mantle composition and processes. *In:* Magmatism in Ocean Basins, A.D. Saunders and M.J. Norry (eds.), Geological Society of London, Special Publication 42, p. 313–345.

Watson, E.B., Wark, D.A. and Thomas, J.B., 2006. Crystallization thermometers for zircon and rutile. Contributions to Mineralogy and Petrology, vol. 151, p. 413–433.

Whalen, J.B., Currie, K.L. and Chappell, B.W., 1987. A-Type granites: Geochemical characteristics, discrimination and petrogenesis. Contribution to Mineralogy and Petrology, vol. 95, p. 407–419.

Witter, J. and Miller, C., 2017. Curie point depth mapping in Yukon. Yukon Geological Survey, Open File 2017-3, 37 p.

Witter, J.B., Miller, C.A., Friend, M. and Colpron, M., 2018. Curie point depths and heat production in Yukon, Canada. Proceedings, 43rd Workshop on Geothermal Reservoir Engineering, Standford University, California, 11 p.

Yukon Geological Survey, 2020a. Yukon Lithogeochemistry data set. Yukon Geological Survey, http://data.geology.gov.yk.ca/Compilation/35#InfoTab, [accessed November 7, 2020].

Yukon Geological Survey, 2020b. Yukon Digital Bedrock Geology. Yukon Geological Survey, http://data.geology.gov.yk.ca/Compilation/3, [accessed November 7, 2020].

Yukon Geological Survey, 2020c. Yukon MINFILE – A database of mineral occurrences. Yukon Geological Survey, http://data.geology.gov.yk.ca/Compilation/24, [accessed November 7, 2020].

Yukon Geological Survey, 2020d. Yukon Geochronology – A database of Yukon isotopic age determinations. Yukon Geological Survey, http://data.geology.gov.yk.ca/Compilation/22, [accessed November 7, 2020].

Appendix 1

U-Pb Geochronology Methods

LA-ICPMS methods

Zircon grains were separated from rocks using standard techniques, annealed at 900°C for 60 hours in a muffle furnace, and mounted in epoxy and polished until their centers were exposed. Cathodoluminescence (CL) images were obtained with a JEOL JSM-300 scanning electron microscope and Gatan MiniCL. Zircon was analyzed by laser ablation inductively coupled plasma mass spectrometry (LA-ICPMS) using a ThermoElectron X-Series II quadrupole ICPMS and New Wave Research UP-213 Nd:YAG UV (213 nm) laser ablation system. In-house analytical protocols, standard materials, and data reduction software were used for acquisition and calibration of U-Pb dates and a suite of high field strength elements (HFSE) and rare earth elements (REE). Zircon was ablated with a laser spot of 25 µm wide using fluence and pulse rates of 5 J/cm^2 and 5 Hz, respectively, during a 45 second analysis (15 sec gas blank, 30 sec ablation) that excavated a pit ~15 µm deep. Ablated material was carried by a 1.2 L/min He gas stream to the nebulizer flow of the plasma. Dwell times were 5 ms for Si and Zr, 200 ms for ^{49}Ti and ^{207}Pb, 80 ms for ^{206}Pb, 40 ms for ^{202}Hg, ^{204}Pb, ^{208}Pb, ^{232}Th, and ^{238}U and 10 ms for all other HFSE and REE. Background count rates for each analyte were obtained prior to each spot analysis and subtracted from the raw count rate for each analyte. Ablation pits that appear to have intersected glass or mineral inclusions were identified based on Ti and P. U-Pb dates from these analyses are considered valid if the U-Pb ratios appear to have been unaffected by the inclusions. Analyses that appear contaminated by common Pb were rejected based on mass 204 being above baseline. For concentration calculations, background-subtracted count rates for each analyte were internally normalized to ^{29}Si and calibrated with respect to NIST SRM-610 and -612 glasses as the primary standards. Temperature was calculated from the Ti-in-zircon thermometer (Watson *et al.*, 2006). Because there are no constraints on the activity of TiO_2, an average value in crustal rocks of 0.8 was used.

Data were collected in one experiment in July 2020 and one in November 2020. For U-Pb and ^{207}Pb/^{206}Pb dates, instrumental fractionation of the background-subtracted ratios was corrected and dates were calibrated with respect to interspersed measurements of zircon standards and reference materials. The primary standard Plešovice zircon (Sláma *et al.*, 2008) was used to monitor time-dependent instrumental fractionation based on two analyses for every 10 analyses of unknown zircon. A secondary correction to the ^{206}Pb/^{238}U dates was made based on results from the zircon standards Seiland (530 Ma, unpublished data, Boise State University) and Zirconia (327 Ma, unpublished data, Boise State University), which were treated as unknowns and measured once for every 10 analyses of unknown zircon. These results showed a linear age bias of several percent that is related to the ^{206}Pb count rate. The secondary correction is thought to mitigate matrix-dependent variations due to contrasting compositions and ablation characteristics between the Plešovice zircon and other standards (and unknowns).

Radiogenic isotope ratio and age error propagation for all analyses includes uncertainty contributions from counting statistics and background subtraction. The standard calibration uncertainty for U/Pb is the local standard deviation of the polynomial fit to the fractionation factor of Plešovice versus time and for ^{207}Pb/^{206}Pb is the standard error of the mean of the fractionation factor of Plešovice. Errors without the standard calibration uncertainty are shown in the data table and are given below for single analyses. For groups of analyses that are collectively interpreted from a weighted mean date (*i.e.*, igneous zircon analyses), a weighted mean date is first calculated from equivalent dates (probability of fit >0.05) using Isoplot 3.0 (Ludwig, 2003) with errors on individual dates that do not include a standard calibration uncertainty. A standard calibration uncertainty is then propagated into the error on the date and is given below. These uncertainties are 0.8–0.9% (2σ) for ^{206}Pb/^{238}U and 0.4–0.5% (2σ) for ^{207}Pb/^{206}Pb. Age interpretations are based on ^{206}Pb/^{238}U dates. Errors are 2σ.

CA-TIMS methods

U-Pb dates were obtained by the chemical abrasion isotope dilution thermal ionization mass spectrometry (CA-TIMS) method from analyses composed of single zircon grains (Table 1), modified after Mattinson (2005). Zircon was removed from the epoxy mounts for dating based on CL images, and before LA-ICPMS data were collected.

Zircon was put into 3 ml Teflon PFA beakers and loaded into 300 ml Teflon PFA microcapsules. Fifteen microcapsules were placed in a large-capacity Parr vessel and the zircon partially dissolved in 120 ml of 29 M HF for 12 hours at 190°C. Zircon was returned to 3 ml Teflon PFA beakers, HF was removed, and zircon was immersed in 3.5 M HNO_3, ultrasonically cleaned for an hour, and fluxed on a hotplate at 80°C for an hour. The HNO_3 was removed and zircon was rinsed twice in ultrapure H_2O before being reloaded into the 300 ml Teflon PFA microcapsules (rinsed and fluxed in 6 M HCl during sonication and washing of the zircon) and spiked with the Boise State University mixed ^{233}U-^{235}U-^{205}Pb tracer solution (BSU-1B). Zircon was dissolved in Parr vessels in 120 ml of 29 M HF with a trace of 3.5 M HNO_3 at 220°C for 48 hours, dried to fluorides, and redissolved in 6 M HCl at 180°C overnight. U and Pb were separated from the zircon matrix using an HCl-based anion-exchange chromatographic procedure (Krogh, 1973), eluted together and dried with 2 µl of 0.05 N H_3PO_4.

Pb and U were loaded on a single outgassed Re filament in 5 µl of a silica-gel/phosphoric acid mixture (Gerstenberger and Haase, 1997), and U and Pb isotopic measurements made on a GV Isoprobe-T multi-collector thermal ionization mass spectrometer equipped with an ion-counting Daly detector. Pb isotopes were measured by peak-jumping all isotopes on the Daly detector for 160 cycles, and corrected for 0.16 ± 0.03%/a.m.u. (1σ) mass fractionation. Transitory isobaric interferences due to high-molecular weight organics, particularly on ^{204}Pb and ^{207}Pb, disappeared within approximately 60 cycles, while ionization efficiency averaged 10^4 cps/pg of each Pb isotope. Linearity (to ≥1.4×10^6 cps) and the associated deadtime correction of the Daly detector were determined by analysis of NBS982. Uranium was analyzed as UO_2^+ ions in static Faraday mode on 10^{12} ohm resistors for 300 cycles, and corrected for isobaric interference of $^{233}U^{18}O^{16}O$ on $^{235}U^{16}O^{16}O$ with an $^{18}O/^{16}O$ of 0.00206. Ionization efficiency averaged 20 mV/ng of each U isotope. U mass fractionation was corrected using the known $^{233}U/^{235}U$ ratio of the Boise State University tracer solution.

U-Pb dates and uncertainties were calculated using the algorithms of Schmitz and Schoene (2007), calibration of BSU-1B tracer solution of $^{235}U/^{205}Pb$ of 77.93 and $^{233}U/^{235}U$ of 1.007066 for, U decay constants recommended by Jaffey et *al.* (1971), and $^{238}U/^{235}U$ of 137.818 (Hiess et *al.*, 2012). $^{206}Pb/^{238}U$ ratios and dates were corrected for initial ^{230}Th disequilibrium using $D_{Th/U} = 0.20 \pm 0.05$ (1σ) and the algorithms of Crowley et *al.* (2007), resulting in an increase in the $^{206}Pb/^{238}U$ dates of ~0.09 Ma. All common Pb in analyses was attributed to laboratory blank and subtracted based on the measured laboratory Pb isotopic composition and associated uncertainty. U blanks are estimated at 0.013 pg.

Weighted mean $^{206}Pb/^{238}U$ dates are calculated from equivalent dates (probability of fit >0.05) using Isoplot 3.0 (Ludwig, 2003). Errors on weighted mean dates are given as ± x / y / z, where x is the internal error based on analytical uncertainties only, including counting statistics, subtraction of tracer solution, and blank and initial common Pb subtraction, y includes the tracer calibration uncertainty propagated in quadrature, and z includes the ^{238}U decay constant uncertainty propagated in quadrature. Internal errors should be considered when comparing our dates with $^{206}Pb/^{238}U$ dates from other laboratories that used the same tracer solution or a tracer solution that was cross-calibrated using EARTHTIME gravimetric standards. Errors including the uncertainty in the tracer calibration should be considered when comparing our dates with those derived from other geochronological methods using the U-Pb decay scheme (e.g., laser ablation ICPMS). Errors including uncertainties in the tracer calibration and ^{238}U decay constant (Jaffey et *al.*, 1971) should be considered when comparing our dates with those derived from other decay schemes (e.g., $^{40}Ar/^{39}Ar$, ^{187}Re-^{187}Os). Errors are 2σ.

Appendix 2 (online only)

CL images of zircon. (PDF)

Appendix 3 (online only)

LA-ICPMS data table (XLS)

Appendix 4 (online only)

Radiogenic heat production data and calculations for the Seagull and Teslin plutonic suite, east of Teslin. (XLS)